ΕΘΝΙΚΟ ΜΕΤΣΟΒΙΟ
ΠΟΛΥΤΕΧΝΕΙΟ

ΣΧΟΛΗ ΕΦΑΡΜΟΣΜΕΝΩΝ
ΜΑΘΗΜΑΤΙΚΩΝ
ΚΑΙ ΦΥΣΙΚΩΝ ΕΠΙΣΤΗΜΩΝ

ΣΧΟΛΗ ΜΗΧΑΝΟΛΟΓΩΝ
ΜΗΧΑΝΙΚΩΝ

ΕΚΕΦΕ «ΔΗΜΟΚΡΙΤΟΣ»

ΙΝΣΤΙΤΟΥΤΟ ΝΑΝΟΕΠΙΣΤΗΜΗΣ
ΚΑΙ ΝΑΝΟΤΕΧΝΟΛΟΓΙΑΣ

ΙΝΣΤΙΤΟΥΤΟ ΠΥΡΗΝΙΚΗΣ ΚΑΙ
ΣΩΜΑΤΙΔΙΑΚΗΣ ΦΥΣΙΚΗΣ

Διατμηματικο Προγραμμα Μεταπτυχιακων Σπουδων
≪ Φυσικη και Τεχνολογικες Εφαρμογες ≫

Mass measurements of J/Ψ and Z at ATLAS Experiment

ΜΕΤΑΠΤΥΧΙΑΚΗ ΔΙΠΛΩΜΑΤΙΚΗ ΕΡΓΑΣΙΑ

της

Μιχαέλας Αραμπατζή

Επιβλέπων:
Θεόδωρος Αλεξόπουλος
Καθηγητής Ε.Μ.Π.

ΑΘΗΝΑ
Ιούνιος 2023

ΕΘΝΙΚΟ ΜΕΤΣΟΒΙΟ
ΠΟΛΥΤΕΧΝΕΙΟ

ΣΧΟΛΗ ΕΦΑΡΜΟΣΜΕΝΩΝ
ΜΑΘΗΜΑΤΙΚΩΝ
ΚΑΙ ΦΥΣΙΚΩΝ ΕΠΙΣΤΗΜΩΝ

ΣΧΟΛΗ ΜΗΧΑΝΟΛΟΓΩΝ
ΜΗΧΑΝΙΚΩΝ

ΕΚΕΦΕ «ΔΗΜΟΚΡΙΤΟΣ»

ΙΝΣΤΙΤΟΥΤΟ ΝΑΝΟΕΠΙΣΤΗΜΗΣ
ΚΑΙ ΝΑΝΟΤΕΧΝΟΛΟΓΙΑΣ

ΙΝΣΤΙΤΟΥΤΟ ΠΥΡΗΝΙΚΗΣ ΚΑΙ
ΣΩΜΑΤΙΔΙΑΚΗΣ ΦΥΣΙΚΗΣ

Mass measurements of J/Ψ and Z at ATLAS Experiment

ΜΕΤΑΠΤΥΧΙΑΚΗ ΔΙΠΛΩΜΑΤΙΚΗ ΕΡΓΑΣΙΑ

της

Μιχαέλας Αραμπατζή

Επιβλέπων: Θεόδωρος Αλεξόπουλος
Καθηγητής Ε.Μ.Π.

Εγκρίθηκε από την τριμελή εξεταστική επιτροπή στις 30 Ιουνίου 2023.

.....	.....	.....
Θ. Αλεξόπουλος	Ε. Γαζής	Σ. Μαλτέζος
Καθηγητής Ε.Μ.Π.	Ομ. Καθηγητής Ε.Μ.Π.	Ομ. Καθηγητής Ε.Μ.Π.

Αθήνα, Ιούνιος 2023

.....
Μιχαέλα Αραμπατζή

Περίληψη

Η παρούσα διπλωματική εργασία εκπονήθηκε στο πλαίσιο της ολοκλήρωσης των μεταπτυχιακών μου σπουδών και αποτελεί μια εισαγωγή στην ανάλυση δεδομένων με στόχο την μελέτη της μάζας του μποζονίου Z και του μεσονίου J/ψ.

Στα πρώτα τέσσερα κεφάλαια, γίνεται μια θεωρητική εισαγωγή κάποιων βασικών εννοιών καθώς και μια μικρή περιγραφή του πειράματος ATLAS, απαραίτητα για την κατανόηση της ανάλυσης που πραγματοποιήθηκε στην παρούσα εργασία.

Στην συνέχεια, η ανάλυση χωρίζεται σε δύο μέρη. Στο πρώτο μέρος, δηλαδή στο κεφάλαιο 5, μελετάται η κατανομή της μάζας του μποζονίου Z, μέσω της διάσπασης $Z \to \mu^+\mu^-$, με σκοπό να βρεθούν οι συναρτήσεις που την περιγράφουν. Αρχικά, χρησιμοποιούνται τα Monte Carlo δεδομένα για την κατασκευή του ιστογράμματος μάζας του Z, μέσω του οποίου βρέθηκε ότι το σήμα περιγράφεται ικανοποιητικά από μια Crystal Ball και από μια Gauss κατανομή ενώ για το υπόβαθρο(background) χρησιμοποιείται ένα πολυώνυμο Chebyshev δευτέρου βαθμού. Εάν και οπτικά η συνάρτηση προσαρμογής φαίνεται να ταιριάζει με την κατανομή μάζας, τα goodness-of-fit tests, δηλαδή τα χ^2/ndf, p-value και pull distribution, φανερώνουν το αντίθετο. Γνωρίζοντας όμως ότι ο ανιχνευτής δεν έχει την ίδια διαριτική ικανότητα σε όλα τα μέρη του και θεωρώντας ότι με τον διαχωρισμό των δεδομένων ανάλογα με την ψευδοωκύτητά τους(pseudorapidity), η, θα υπάρξει βελτίωση της διαδικασίας του fit, χωρίζουμε τον ανιχνευτή σε 11 η-περιοχές μεταξύ των [-1.1,1.1]. Επομένως, επειδή το καθε μυόνιο από τα δύο μπορεί να ανιχνευθεί σε μια από τις 11-η περιοχές, δημιουργούνται 11×11 ιστογράμματα μάζας άρα και συναρτήσεις προσαρμογής (fit). Η σκέψη αυτή επιβεβαιώθηκε καθώς αφού έγινε ο η διαχωρισμός των μυονίων οι συναρτήσεις προσαρμογής βελτιώθηκαν σημαντικά για όλους τους συνδυασμούς των η-περιοχών που μπορούν να ανιχνευτούν τα δυο παραγώμενα μυόνια, δηλαδή για όλα τα 11×11 ιστογράμματα. Το επόμενο βήμα ήταν να εξετασθεί εάν ο διαχωρισμός των δεδομένων σε 11 η-περιοχές επηρεάζει τη στατιστική τής ανάλυσης, κάτι που επιβεβαιώθηκε. Καταληκτικά, μελετήθηκε η σχέση των παραμέτρων που βρέθηκαν από τις διάφορες συναρτήσεις προσαρμογής με τις η περιοχές όπου ανιχνεύονται τα δυο μυόνια από την διάσπαση του μποζονίου Z, η οποία φανέρωσε συστηματικό σφάλμα. Αφού έγινε όλη η ανάλυση στα MC δεδομένα, εφαρμόζουμε το ίδιο μοντέλο και την ίδια μεθοδολογία στα δεδομένα έτσι ώστε να συγκριθούν τα αποτελέσματα μεταξύ τους. Σε κάποια αποτελέσματα υπάρχουν διαφορές οι οποίες λογικά υποδηλώνουν ότι τα MC χρειάζονται κάποιες

αλλαγές.

Στο δεύτερο μέρος της ανάλυσης, δηλαδή στο 6ο κεφάλαιο, στόχο έχουμε να συμβάλλουμε στην προσπάθεια ακριβούς μέτρησης της μάζας του μποζονίου Z, μέσω της διάσπασης $Z \to \mu^+\mu^-$. Η επιδίωξη μιας ακριβούς μέτρησης έχει οδηγήσει τις μελέτες να εστιάσουν στη βελτίωση της βαθμονόμησης της ενέργειας των μυονίων. Στο πλαίσιο αυτό, προτείνεται μια νέα μεθοδολογία βαθμονόμησης, η οποία βασίζεται στα διαγράμματα Armenteros-Podolanski. Το διάγραμμα Armenteros-Podolanski είναι μια αναπαράσταση της εγκάρσιας ορμής μιας διάσπασης ουδέτερων σωματιδίων σε δυο σωματίδια ως προς την ασυμμετρία της διαμήκους ορμής των προϊόντων της διάσπασης. Η μέθοδος στηρίζεται στον προσδιορισμό των μαζών των σωματιδίων της τελικής κατάστασης και γι'αυτό τον λόγο προτείνεται ως μέθοδος καθώς θεωρείται ότι επιτρέπει μια σημαντικά ακριβέστερη βαθμονόμηση της ορμής από τη χρήση μόνο των μητρικών σωματιδίων, εφόσον οι μάζες των τελικών σωματιδίων είναι γνωστές με μεγαλύτερη ακρίβεια από ότι αυτές των μητρικών σωματιδιών. Αρχικά, αποδεικνύεται η μαθηματική έκφραση των διαγραμμάτων Armenteros-Podolanski και έπειτα εξετάζεται η συμπεριφορά της για μικρές και μεγάλες μάζες, χρησιμοποιώντας δεδομένα J/ψ και Z αντίστοιχα. Αφού έχει κατανοηθεί η συμπεριφορά της εξίσωσης, εφαρμόζουμε δυο δοκιμασίες στα διαγράμματα Armenteros-Podolanski, για να εξετασθεί εάν τα διαγράμματα ανταποκρίνοται επιτυχώς σε αυτές, κάτι το οποίο επιτυγχάνεται. Επομένως, συμπεραίνεται ότι τα διαγράμματα Armenteros-Podolanski θα μπορούσαν, έπειτα και από επιπλέον έρευνα, να αποτελέσουν μια μέθοδο η οποία να χρησιμοποιείται για την βαθμονόμηση του ανιχνευτη επιτρέποντας μάλιστα μια σημαντικά ακριβέστερη βαθμονόμηση.

Abstract

The present thesis was written in the context of my master's studies and is an introduction to data analysis in order to study the mass of the boson Z and the J/ψ meson.

In the first four chapters, a theoretical introduction of some basic concepts and a brief description of the ATLAS experiment is given, necessary for the understanding of the analysis carried out in this thesis.

Then, the analysis is divided into two parts. In the first part, i.e. chapter 5, the mass distribution of the boson Z, through the decay $Z \to \mu^+\mu^-$, is studied in order to find the functions describing it. Firstly, Monte Carlo data are used to make the Z mass histogram, through which it is found that the signal is satisfactorily described by a Crystal Ball and a Gaussian distribution, while a second-degree Chebyshev polynomial is used for the background. Although visually the fit seems to correspond to the mass distribution, the goodness-of-fit tests, i.e. χ^2/ndf, p-value and pull distribution, reveal the opposite. However, knowing that the detector does not have the same resolution in all its parts and expecting that separating the data according to their pseudorapidity, η, will improve the fit procedure, we divide the detector into 11 η-regions between [-1.1,1.1]. So, because each of the two muons can be detected in any of the 11-η-regions, 11×11 mass histograms and their corresponding fit are produced. This idea was confirmed as after performing the η separation of the muons, the fit procedure improved significantly for all combinations of η-regions, where the two produced muons can be detected, i.e. for all 11×11 histograms. The next step was to examine whether the separation of the data into 11 η-regions affects the statistics of the analysis, which was confirmed. Last, we studied the relationship between the fitted parameters and the η regions where the two muons from the Z boson decay are detected, which revealed a systematic error. After carrying out all the analysis on the MC data, we apply the same model and the same methodology to the data in order to compare the results with MC's ones. In some results there are differences which logically indicate that the MC data need some improvements.

In the second part of the analysis, i.e. chapter 6, the objective is to contribute to the attempt to measure precisely the mass of the boson Z, through the decay $Z \to \mu^+\mu^-$. The pursuit of a precise measurement has led studies to focus on improving the calibration of muon energy. In this context, a new calibration method is suggested, based on the Armenteros-Podolanski plots. The Armenteros-Podolanski

plot is a representation of the transverse momentum of a two-body decay versus the asymmetry of the longitudinal momentum of the decay products. The method is based on the determination of the masses of the final state particles and for this reason it is proposed as a method because it is believed that it allows a significantly more accurate calibration of the momentum than using only the parent particles, since the masses of the final particles are known more precisely than those of the parent particles. Firstly, the mathematical expression of the Armenteros-Podolanski plots is demonstrated and then its behaviour for small and large masses is examined, using J/ψ and Z data respectively. Once the behavior of the equation has been understood, we apply two tests to the Armenteros-Podolanski plots to check whether the plots successfully respond to them, which is achieved. Therefore, it is inferred that the Armenteros-Podolanski plots could, after further research, be a method to be used for the calibration of the detector and even provide a significantly more accurate calibration.

Ευχαριστίες

Θα ήθελα να ευχαριστήσω ιδιαιτέρως τον Καθηγητή μου κ. Αλεξόπουλο Θεόδωρο, ο οποίος με υπομονή, θετική διάθεση και πολύτιμη καθοδήγηση με βοήθησε να κατανοήσω και να εξοικειωθώ με τις έννοιες της φυσικής υψηλών ενεργειών και την ανάλυση δεδομένων καθώς και την ευκαιρία που μου έδωσε να ασχοληθώ με το συγκεκριμένο θέμα.

Ένα μεγάλο ευχαριστώ οφείλω στον Ερευνητή κ. Ανδρέα Ψαλλίδα στο Ινστιτούτο Πυρηνικής και Σωματιδιακής Φυσικής στο ΕΚΕΦΕ ≪Δημόκριτος≫, για την πολύτιμη βοηθειά του στην ανάλυση δεδομένων και για τις πολύ ωραίες συζητήσεις μας επάνω στην φυσική στοιχειωδών σωματιδίων.

Θα ήθελα, επίσης, να ευχαριστήσω τον υποψήφιο Δρ. κ. Διονύσιο Φακούδη για τη βοήθεια που μου προσέφερε κατά την διάρκεια της εκπόνησης της διπλωματικής μου εργασίας καθώς και τον μεταπτυχιακό φοιτητή κ. Στέλιο Χρηστινάκη για τις πολύτιμες συμβουλές του στο προγραμματισμό αλλά και για τις συζητήσεις μας στις ώρες διαβάσματος για την ολοκλήρωση των μεταπτυχιακών μας σπουδών.

Ευχαριστώ πολύ τις φίλες και τους φίλους μου που ήταν πάντα δίπλα μου όλα τα εκπαιδευτικά χρόνια και κυρίως αυτή την περίοδο της εκπόνησης της διπλωματικής μου εργασίας.

Τέλος, ένα μεγάλο ευχαριστώ στην οικογένειά μου, τους γονείς μου Γιώργο και Κατερίνα και την αδελφή μου Δήμητρα, για την αμέριστη αγάπη και στήριξή τους.

Acknowledgments

I would like to thank especially my Professor Mr. Theodoros Alexopoulos, who with patience, kind disposition and valuable guidance helped me to understand and familiarize with the concepts of high energy physics and data analysis and gave me the opportunity to work on the topic.

My thanks to Researcher Mr. Andreas Psallidas of the Institute of Nuclear and Particle Physics at NSCR ≪Demokritos≫, for his valuable help in data analysis and for our fruitful discussion on elementary particle physics.

I would also like to thank the doctoral candidate Mr. Dionysios Fakoudis for his help during the preparation of my thesis and the postgraduate student Mr. Stelios Christinakis for his valuable advice on programming and for our discussion during study hours for the completion of our master studies.

I am very grateful to my friends who have always been by my side throughout my studies and especially during the time of preparing my thesis.

Finally, a big thanks to my family, my parents Georgios and Katerina and my sister Dimitra, for their unconditional love and support.

Contents

Chapter 1

The Standard Model

Particle physics is at the heart of understanding the laws of nature. It deals with the fundamental components of the Universe, the elementary particles and the interactions between them, i.e. the forces. Our present understanding is integrated in the Standard Model of particle physics, which provides a unified picture where the forces between particles are described by the exchange of particles. The theory of the Standard Model can provide predictions for the vast majority of observed data up to the energy regime of the LHC. [1],[2],[3]

1.1 Particles

Particles are divided according to their spin into two categories, fermions and bosons. Fermions are the particles of matter and they are spin particles, so they follow Fermi-Dirac statistics. Fermions are further divided into two classes, leptons and quarks. Leptons interact with the electromagnetic and weak forces and they consist of three generations. Each generation consists of two particles, one negatively electrically charged which interacts with both the electromagnetic and weak forces (electron, muon and tau lepton) and the other is the corresponding neutrino which interacts only with the weak force as it has zero electric charge. The above together with their antiparticles form the lepton part of the Standard Model. On the other hand, quarks interact through the strong, weak and electromagnetic forces. Quarks, like fermions, consist of three generations. Each generation of quarks consists of two particles, an upper type quark which has a positive electric charge equal to $+\frac{2}{3}$ and a lower type quark which has a negative electric charge equal to $-\frac{1}{3}$.

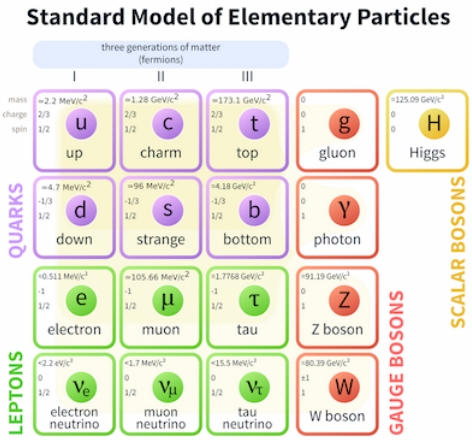

Figure 1.1: Particles of the Standard Model

1.2 Interactions

In the modern particle physics, each force is described by a Quantum Field Theory, according to which, as mentioned earlier, the interaction between particles takes place through a force, carried by bosons. So far, four forces are known to exist in nature: the gravitational, the electromagnetic, the strong and the weak forces. However, the quantum theory is able to describe three of these four forces because the boson which is carried by the gravitational force, known as the graviton, has not been discovered experimentally. For this reason, the gravitational force has not been included in the Standard Model. The three interactions are described by the following respective theories: the Quantum Chromodynamics theory (QCD) for the strong force, the Quantum Electrodynamics theory (QED) for the electromagnetic force and the Electro - weak Theory (EW) for the electroweak force, which unifies the electromagnetic and the weak forces. QED introduces the massless photon as the propagator of the electromagnetic force. The strong force is applied to particles that have a colour charge and is described by the Quantum Chromodynamics theory (QCD), which introduces 8 massless gluons as its propagators. Finally, the weak force is the force with which all fermions interact and its propagators are the charged bosons $W\pm$ and the neutral Z^0.

1.3 Boson Z

The main topic of this thesis is the Z boson of which a description will be given below.
A consequence of the electroweak model is the prediction of a weak neutral current carried by the neutral Z bosons. The Z boson, like $W\pm$, carries the weak force. It was predicted the-

oretically in the 1960s, and discovered in 1983 by physicists at the Super Proton Synchrotron (SPS).

As the Z boson is a neutral elementary particle, the total charge of the particles into which it decays should be zero due to the conservation of electric charge in nature. Therefore, Z bosons decay into fermion pairs of the same family, i.e. a particle-antiparticle pair. For example, some illustrative decays of the Z boson are the following:

(a) Decay of a Z particle into an electron-positron pair

(b) Decay of a Z particle into a muon-anti-muon pair

Figure 1.2: Examples of boson Z decay

In the unified electroweak model, the photon and Z boson are written as linear combinations of the B_μ and neutral $W_\mu^{(3)}$ of the weak interaction:

$$A_\mu = +B_\mu \cos\theta_W + W_\mu^{(3)} \sin\theta_W$$

$$Z_\mu = -B_\mu \sin\theta_W + W_\mu^{(3)} \cos\theta_W$$

where θ_W is the weak mixing angle.
As for boson B, it corresponds to a new symmetry, the $U(1)_y$ Hypercharge. This new symmetry is analogous to the symmetry of the electromagnetic interaction. The boson B couples to a new kind of charge called weak hypercharge Y, which is a linear combination of the electromagnetic charge Q and the third component of the weak isospin $I_w^{(3)}$:

$$Y = 2(Q - I_w^{(3)})$$

Thus, the Z boson couples to both right-handed (RH) and left-handed (LH) chiral states, in contrast to bosons $W^\pm$ which interact only with left-handed particles and right-handed antiparticles, but not equally because it is associated with different constants depending on the state, and specifically:

$$c_L = I_W^{(3)} - Q_f \sin^2\theta_W$$

$$c_R = -Q_f \sin^2 \theta_W$$

The description of the Z boson coupling can also be achieved in vector and axial-vector terms as follows:

$$c_V = c_L + c_R = I_W^{(3)} - 2Q_f \sin^2 \theta_W$$

$$c_R = c_L + c_R = I_W^{(3)}$$

In terms of these vector and axial-vector couplings, the Feynman rule associated with the Z-boson interaction vertex is:

$$-i\frac{1}{2}g_Z\gamma^\mu \left[c_V - c_A\gamma^5\right]$$

The Z boson couples to all fermions so it can decay to all leptons and all flavours of quarks except of the top quark because its mass, $m_t = 175$ GeV, is bigger than the mass of Z ($m_t > m_Z$).
The partial decay rate to a particular fermion flavour can be calculated from the equation:

$$\Gamma(Z \to f\bar{f}) = \frac{g_Z^2 m_Z}{48\pi}\left(c_v^2 + c_A^2\right)$$

using the appropriate vector and axial-vector couplings:

$fermion$	c_L	c_R	c_V	c_A
ν_e, ν_μ, ν_τ	$+\frac{1}{2}$	0	$+\frac{1}{2}$	$+\frac{1}{2}$
e^-, μ^-, τ^-	$-0{,}27$	$+0{,}23$	$-0{,}04$	$+\frac{1}{2}$
u, c, t	$+0{,}35$	$-0{,}15$	$+0{,}19$	$+\frac{1}{2}$
d, s, b	$-0{,}42$	$+0{,}08$	$-0{,}35$	$+\frac{1}{2}$

Figure 1.3: The values of the constants c_L, c_R, c_V, c_A of the fundamental fermions for finding their couplings with Z assuming $\sin^2 \theta_w$

Knowing that the total decay width Γ_Z is occured by the sum of the partial decay widths

$$\Gamma_Z = \sum_f \Gamma(Z \to f\bar{f})$$

and also that the Z-boson couplings, as shown in Fig.1.3, are the same for all three generations, it arises that:

$$\Gamma_Z = 3\Gamma(Z \to \nu_e\bar{\nu_e}) + 3\Gamma(Z \to e^+e^-) + 3 \times 2\Gamma(Z \to u\bar{u}) + 3 \times 3\Gamma(Z \to d\bar{d})$$

and thus it is calculated to be $\Gamma_Z = 2.5$ GeV and the branching ratios of the Z boson, given by $Br(Z \to f\bar{f}) = \Gamma(Z \to f\bar{f})/\Gamma_Z$, are:

$$Br(Z \to \nu_e\bar{\nu_e}) = Br(Z \to \nu_\mu\bar{\nu_\mu}) = Br(Z \to \nu_\tau\bar{\nu_\tau}) \approx 6.9\%$$

$$Br(Z \to e^+e^-) = Br(Z \to \mu^+\mu^-) = Br(Z \to \tau^+\tau^-) \approx 3.5\%$$

$$Br(Z \to u\bar{u}) = Br(Z \to u\bar{u}) \approx 12\%$$

$$Br(Z \to d\bar{d}) = Br(Z \to s\bar{s}) = Br(Z \to b\bar{b}) \approx 15\%$$

Grouping together the decays to neutrinos, charged leptons, and quarks gives

$$Br(Z \to \nu\bar{\nu}) \approx 21\%, Br(Z \to l^+l^-) \approx 10\%, Br(Z \to hadrons) \approx 69\%$$

and so almost 70% of Z decays have as final states jets. [1]

From data taken up to the end of 1990 by the four LEP collaborations ALEPH, DELPHI, L3 and OPAL, a combined value of m_Z had been obtained in 1993, which is $m_Z = 91.1876 \pm 0.0021$ GeV.

Chapter 2

The Large Hadron Collider and the ATLAS detector

2.1 CERN

CERN (Conseil Européen pour la Recherche Nucléaire) [4] is an intergovernmental particle physics research organization composed of 23 member states. The original convention establishing CERN was signed in 1953 by the first 12 founding members (Belgium, Denmark, France, the Federal Republic of Germany, Greece, Italy, the Netherlands, Norway, Sweden, Switzerland, the United Kingdom and Yugoslavia) and entered into force on 29 September 1954.The headquarters of the organization is located in Geneva, although its facilities are shared on both sides of the Franco-Swiss border. The organization has as its mission the international cooperation in the field of high-energy research or particle physics and to this end, it builds and puts into operation particle accelerators together with suitable experimental detector facilities for the detection of the products of either beam collisions with a fixed target or bonds between them.

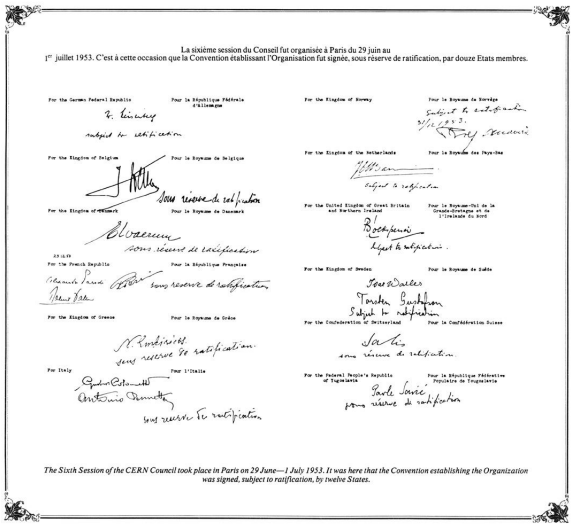

La sixième session du Conseil fut organisée à Paris du 29 juin au 1er juillet 1953. C'est à cette occasion que la Convention établissant l'Organisation fut signée, sous réserve de ratification, par douze Etats membres.

The Sixth Session of the CERN Council took place in Paris on 29 June—1 July 1953. It was here that the Convention establishing the Organization was signed, subject to ratification, by twelve States.

Figure 2.1: The Convention establishing CERN

Today CERN has 23 Member States: Austria, Belgium, Bulgaria, Czech Republic, Denmark, Finland, France, Germany, Greece, Hungary, Israel, Italy, Netherlands, Norway, Poland, Portugal, Romania, Serbia, Slovak Republic, Spain, Sweden, Switzerland and United Kingdom.

2.2 Accelerator complex

The accelerator complex at CERN is a succession of machines that accelerate particles to increasingly higher energies. Each machine boosts the energy of a beam of particles before injecting it into the next machine in the sequence.

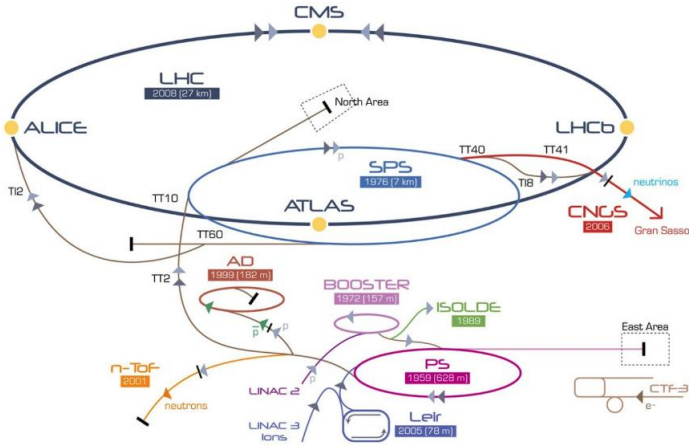

Figure 2.2: The CERN accelerator complex

The most recent addition is the Large Hadron Collider (LHC). The existing accelerator chain (Linac → Booster → PS → SPS) will be used to inject protons into the LHC as shown in the Fig.2.2. Protons will be produced and accelerated to 50 MeV by the Linear Accelerator (Linac) before being injected into the Booster giving them an energy of 1.4 GeV. The Proton Synchrotron (Proton Synchrotron or PS) will then accelerate the protons to 26 GeV and finally the SPS (Super Proton Synchrotron) will provide protons with an energy of 450 GeV which will be injected into the LHC.

2.3 The LHC

The Large Hadron Collider (LHC) is the largest and most powerful particle accelerator in the world. It first started up on 10 September 2008, and remains the latest addition to the CERN's accelerator complex. The LHC is a circular collider with a circumference of 27 kilometres located about 100 metres below the Earth's surface. The LHC is capable of accelerating two counter-rotating beams of protons (and Pb (lead) ions) with energies of up to an energy of 7 TeV per beam.

2.3.1 Luminosity

One of the most important parameters of an accelerator is its luminosity which is measuring the number of collisions per unit time. What makes luminosity important in particle accelerator experiments is relation (2.1) which connects the number of events per second created in such an experiment with luminosity and the cross-section σ of the particle reaction under study. Particularly, the rate of interaction $\frac{dN}{dt}$, i.e. the number of interactions N per sec is given by:

$$\frac{dN}{dt} = \sigma \mathscr{L} \tag{2.1}$$

in which σ is the cross-section of the process of interest, describing the probability of the interaction and $\mathscr{L}$ is the instantaneous luminosity. The instantaneous luminosity is measured in units $cm^{-2}s^{-1}$.

However, the particles in an accelerator are not distributed evenly throughout the accelerator, but they are grouped into bunches. So, the instantaneous luminosity of the machine can be expressed in terms of the numbers of particles in the colliding bunches, n_1 and n_2, the frequency at which the bunches collide, and the root-mean-square(rms) horizontal and vertical beam sizes σ_x and σ_y:

$$\mathscr{L} = f\frac{n_1 n_2}{4\pi\sigma_x\sigma_y}$$

The integrated luminosity is obtained, by integrating the instantaneous luminosity over the accelerator active time, and it associates the total number of produced events N_{tot} to the pp cross-section:

$$N_{tot} = \sigma \int \mathscr{L}\, dt$$

and its unit is $barn^{-1}$. [1]

2.3.2 The LHC experiments

In the largest part of the LHC ring the two beams travel in two separate vacuum tubes, except for four points where they collide. These points are where take place the main LHC experiments, known by their acronyms ALICE, ATLAS, CMS and LHCb [5].

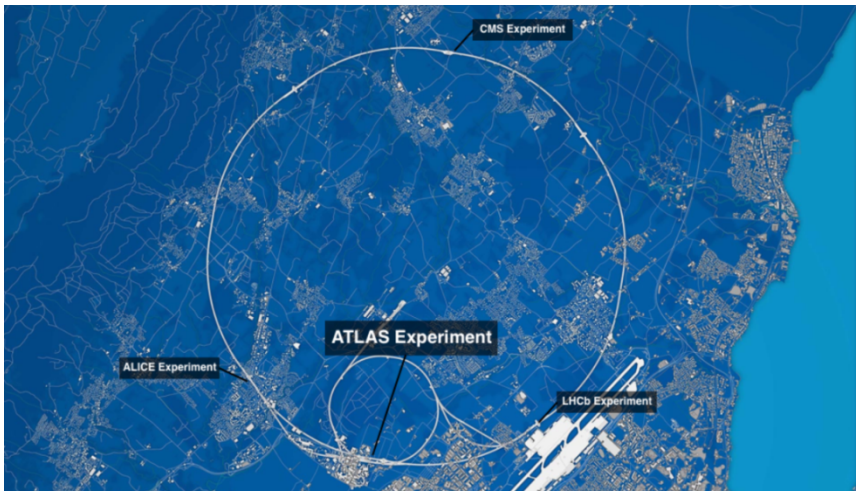

Figure 2.3: The LHC experiments

The four main experiments have different scientific goals and are briefly presented below:

- **ALICE (A Large Ion Collider Experiment):** a general-purpose detector for heavy-ion physics, which is designed to study the physics of strongly interacting matter and the quark-gluon plasma at extreme values of energy density and temperature.
- **ATLAS(A Torroidal LHC ApparatuS):** a general-purpose experiment with a broad physics research program, from the Higgs boson to extra dimensions and particles

that could make up dark matter. More detailed discription of ATLAS is given to the next chapter.

- **CMS(Compact Muon Solenoid):** a general-purpose experiment with the same scientific goals as the ATLAS but which differs completely from the latter in the design principle.

- **LHCb:** an experiment focused to b-physics studies, precision measurements of CP violation and B-meson decays.

There are other smaller experiments on the LHC, which are TOTEM, LHCf, MoEDAL-MAPP, FASER and SND@LHC. In particular, TOTEM and LHCf focus on "forward particles" - protons or heavy ions that pass each other rather than meeting head on when the beams collide. TOTEM uses detectors which are on both sides of the CMS, while LHCf is located at 140 metres either side of ATLAS. MoEDAL-MAPP uses detectors which are near LHCb in order to search for a hypothetical particle called the magnetic monopole. FASER and SND@LHC, the two newest LHC experiments, are situated close to ATLAS to search for light new particles and to study neutrinos.

2.4 The ATLAS detector

ATLAS [6], [7] is one of the four big experiments of LHC. Geometrically, ATLAS has a cylindrical shape with 4π coverage and dimensions of 46 m lenght, 25 m high and 25 m wide while it weighs 7000 tonnes. It is located in a cavern 100 m under the ground near the main CERN site, close to the village of Meyrin in Switzerland. ATLAS is a general purpose experiment and as such is designed to take full advantage of LHC's potential. Its design aims to detect the particles which are produced in proton-proton (p-p) collisions at the LHC.

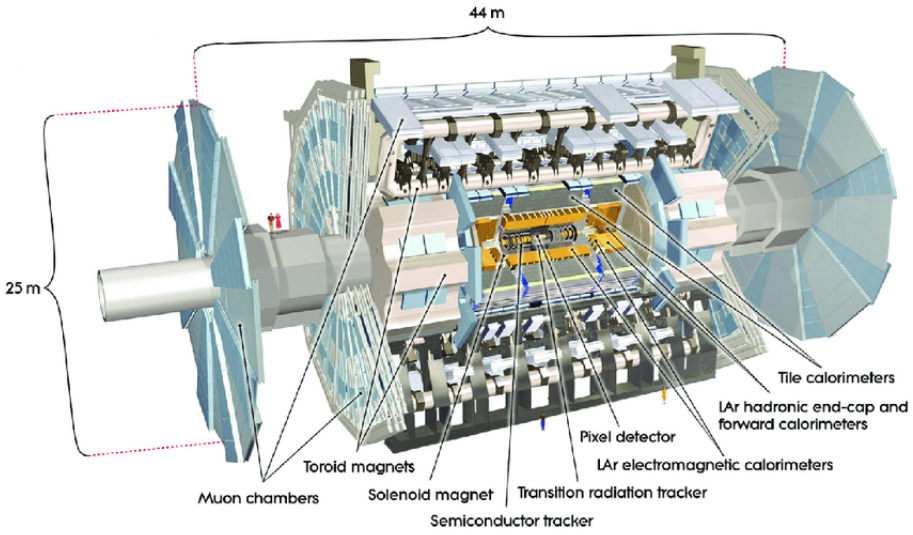

Figure 2.4: Cut-away view of the ATLAS detector - Also the different detector sub-systems are illustrated

2.5 Structure

The main parts of the ATLAS detector are the sub-detectors and the magnet system.

2.5.1 Sub-detectors

The ATLAS detector consists of four different sub-detectors that are arranged in different planes around the z-axis, where the collisions take place. The main ones from the inside out are the following:

1. Inner Detector
2. Electromagnetic Calorimeter
3. Hadronic Calorimeter
4. Muon Spectrometer

Specifically, the ***Inner Detector*** is the innermost part of the ATLAS detector. It has a length of 6.2 m, a radius of 1.2 and it is immersed inside the 2 T magnetic field formed by the central solenoid, which will be described further below. This magnetic field causes the curvature of the trajectories of the charged particles. The Inner Detector measures, from the direction and degree of curvature, the direction, momentum and charge of the electrically charged particles that are produced in each proton collision. Thus, its main function is to

detect charged particles and their interaction with matter; by this way information on the momentum and type of particles is obtained. It is divided in three systems which, in order of radial distance from the collision point, are: the Pixel Detector, the Semiconductor Tracker (SCT) and the Transition Radiation Tracker (TRT). Continuing, and moving towards the outer levels of the detector, the calorimeters are dispayed. The ATLAS Calorimetric System is located between the Inner Detector and the Muon Spectrometer and is divided into two main categories, the electromagnetic and the hadronic calorimeter. The objective of the ATLAS Calorimetric System is to measure as precise as possible the energy of electrons, photons and jets and to provide information on the missing transverse energy ($E_{T_{miss}}$). Firstly, the ***electromagnetic calorimeter*** is found which measures the energy of electrons and photons as they interact with matter and secondly the ***hadronic calorimeter*** which measures the energy of hadrons as they interact with atomic nuclei. Calorimeters can stop most known particles except muons and neutrinos. Also, it is important to note that because of the use of calorimeters, which is the absorption of the particle's energy, the calorimeters are located outside the inner detector so that the charged particle's trajectory is recorded before being absorbed by the calorimeter. Further on, the calorimeters are surrounded by the ***Muon Spectrometer***. The ATLAS muon detector system is designed to provide independent measurement of the energy and trajectory of the muons with high accuracy. This is because muons are particles that normally pass through the inner detector and the calorimetric system without being detected. It consists of two types of detection systems, the triggering system and the high-precision tracking system. The description of the detector structure which was presented earlier, is portrayed in the image shown below:

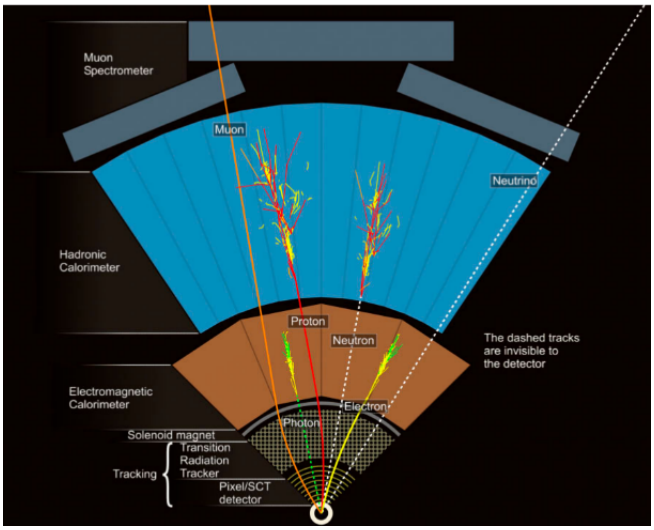

Figure 2.5: Sub-detector system of ATLAS

2.5.2 The Magnet System

ATLAS experiment uses an impressive magnet system [8] in order to bend the trajectories of charged particles and, by measuring their deflection, to define their momentum. It consists of one superconducting central solenoid placed around the Inner Detector cavity and three superconducting toroids, one in the barrel and two in the end-cap regions. Thus, the main sections of the magnet system are:

- the Central Solenoid
- the Barrel Toroid
- two air-core Endcap Toroids

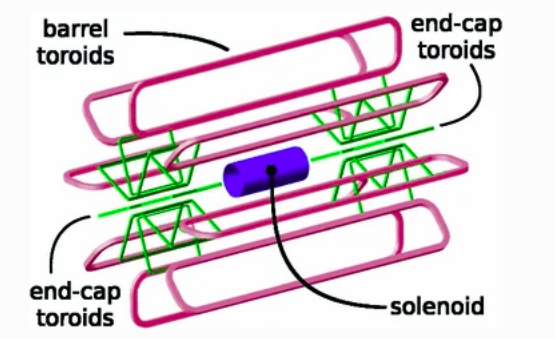

Figure 2.6: View of the complete ATLAS Magnet System

The *Central Solenoid* encloses the Inner Detector and is enclosed by the calorimetric system. It is of 5.3 m length and operates at a nominal current of 7.73 kA. The result is an axial magnetic field of 2 T in the z direction, bending the trajectories of charged particles in the ϕ direction.

Figure 2.7: The Central Solenoid magnet

Continuing, the *toroidal magnet* is divided into the barrel section and the end-caps section. Both are located outside the calorimeters but inside the muon spectrometer, they are used to provide a magnetic field to the muons and thus bend their trajectories. The barrel section consists of 8 coils arranged symmetrically around the beam axis and the two side magnets also contain 8 coils each.

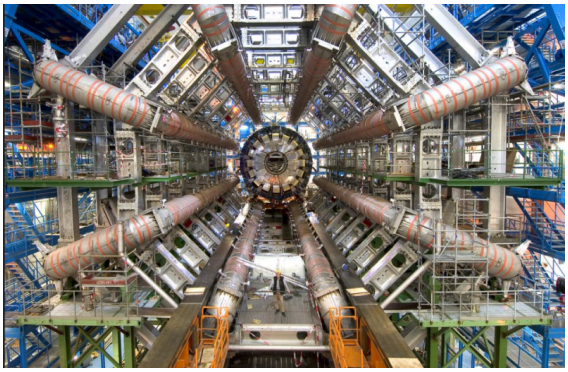

(a) Barrel Toroid

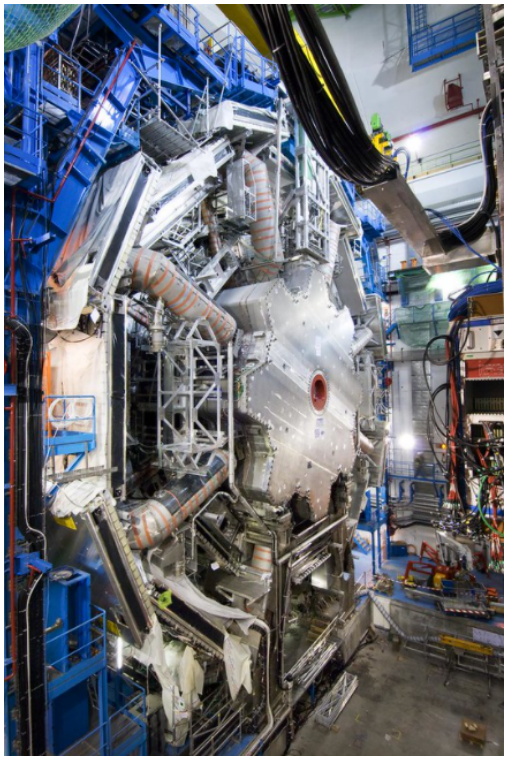

(b) End-cap Toroid

Figure 2.8: Toroid Magnet

2.5.3 Coordinate System

The ATLAS reference system is a cartesian right-handed coordinate system. The reference point is the nominal interaction point (IP) in the centre of the detector. The z-axis is defined by the beam direction, the positive x-axis points from the IP to the centre of the LHC ring and the y-axis points upwards and thus the xy plane is perpendicular to the beam axis.

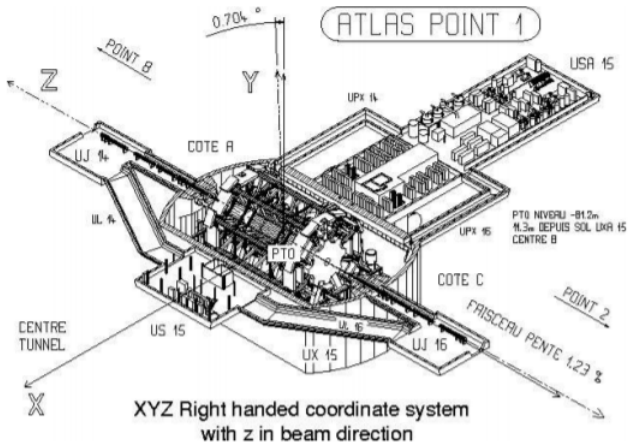

Figure 2.9: The cartesian coordinate system of the ATLAS detector

Because of the detector geometrical design, cartesian coordinates are not practical and thus polar coordinates are used. Specifically, R is the distance from the reference point (IP), θ $[0, \pi)$ is the polar angle from the z axis and ϕ $[-\pi, \pi]$ the azimuthal angle which runs around z axis.

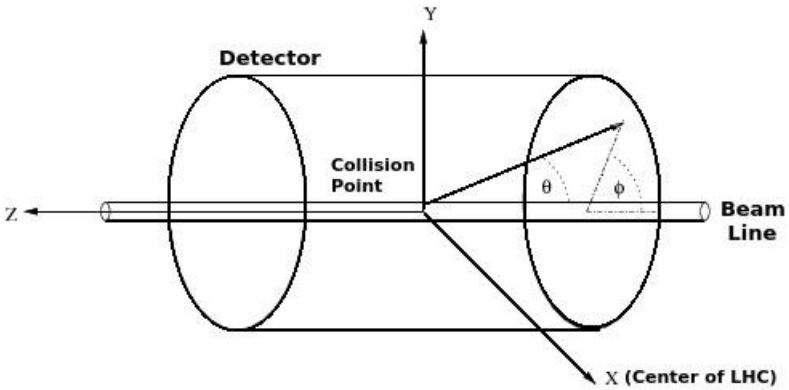

Figure 2.10: The polar coordinates of the ATLAS detector

Due to the fact that the colliding partons have unknown momentum in each collision, the total momentum along the z axis is not known. Consequently, the momentum conservation between the initial and final states can not be applied along the z axis, it can only be applied to the transverse plane, defined as the projection on the xy plane. For this reason, important quantities like momentum and energy are usually given in the transverse plane xy:

$$p_T = Psin\theta \tag{2.2a}$$

$$E_T = Esin\theta \tag{2.2b}$$

Another important quantity that is widely used in particle physics experiments is the rapidity y which is defined by:

$$y = \frac{1}{2} \ln \left(\frac{E + p_z}{E - p_z} \right) \tag{2.3}$$

where E is the energy of the particle and p_z is its momentum component in the z-direction. However, when we study particles with negligible mass, the relation (2.3) is simplified, so we can use the pseudorapidity η, which is defined by:

$$\eta = - \ln \left(tan \frac{\theta}{2} \right) \tag{2.4}$$

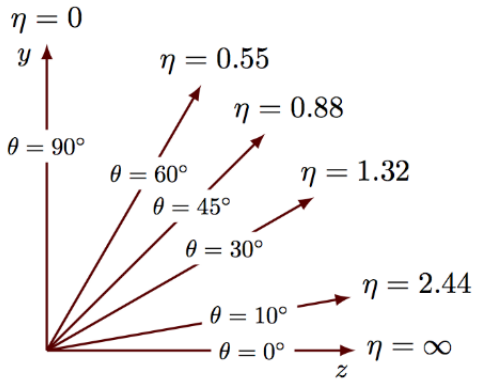

Figure 2.11: Pseudorapidity

Once the pseudorapidity η and the azimuthal angle ϕ have been defined, the angular distance R between two particles in space $\eta - \phi$, can be defined by:

$$\Delta R = \sqrt{\Delta\eta^2 + \Delta\phi^2} \tag{2.5}$$

Chapter 3

Blind Analysis

We give the "Clever Hans" [9] example below to illustrate the significance of bias in an experiment. Hans von Osten, who lived at the beginning of the 20th century, had math skills. Given a pair of single-digit numbers written on a blackboard, Hans could add them together correctly almost all the time. The extraordinary thing about this fact is that Hans was a horse. So, in front of those who had come up with the dilemma, Hans would show off his prowess by pounding the ground with his hoof until he reached the sum of the two numbers.

Critics of Hans' skills were trying to determine if his trainer was providing the answer with signals, but they could find none. Finally, they asked the trainer to leave the room, but Hans was still able to add the numbers most of the time. The mystery of Hans' ability was not solved until 1907, when the psychologist Oskar Pfungst proposed a test in which no one in the room but Hans knew the given two numbers. With all the observers unaware of the solution, Hans was unable to give the right answer. The conclusion was that Hans was surely clever since he had exploited subtle non-verbal cues from those in the room – cues that his observers were not even aware that they were giving – to choose when to stop treading on the ground.

The phenomenon of "Clever Hans" left its imprint on modern science, particularly medicine. Most large-scale clinical trials for new drugs require that not only the participants be unaware of whether they are taking a placebo or not, but also that those dispensing the medication remain unaware of which individuals make up the control group, so the trials are double-blind.

Blind analysis is a method that hides some aspect of the data or outcome to counteract

the experiment's bias. No single blind analysis method exists, nor is every technique suitable for all measurements. The experiment and the blind analysis method, on the other hand, must be well matched, both to prevent the experimenter's bias and to allow the measurement to be carried out unobstructed by the method. There are various blind analysis methods, each of which is suitable for a particular type of measurement. These methods can be categorized according to precisely what is hidden in the measurement:

1. The signal events, when the signal occurs in a well-defined region of the experiment's phase space.
2. The result, when the numerical answer can be separated from all other aspects of the analysis.
3. The number of events in the data set, when the answer relies directly upon their count.
4. A fraction of the entire data set.

However, only the first method will be analyzed, known as the Hidden Signal Box methodology, as it is perhaps the most straightforward blind analysis method and the one used most frequently in CERN experiments' analyses. Furthermore, the analysis developed below for studying the muon momentum calibration in the mass regions of J/ψ is based on the logic of this method.

3.1 Hidden Signal Box

In this technique, a subset of the data containing the potential signal is kept hidden until all aspects of the analysis are completed. In CERN experiments, research is conducted to search for new particles by looking for signals within a background of known physics. If the data start to indicate something more interesting than the simple background - for example, more decay events than expected in a specific region - it is important to ensure that the observation is statistically significant by collecting and analyzing more data. However, we do not want to predetermine our analyses by optimizing them based on what has already been observed. To avoid such bias in the analysis of new data, physicists design "blinds" over the region where an excess of decay events is expected. This region is "unblinded" only when they are satisfied with their procedures. This ensures objectivity when searching for the coveted signs of new physics and instills confidence in the final result. Thus, blind analysis avoids the possibility for experimenters to direct their results towards their own preconceived

ideas, preventing them from knowing the answer until the analysis is completed.

This is also the reason why the analysis, which aims to precisely measure the mass of Z boson - therefore the object of study -, uses blinding in the signal region, and the analysis methodology is tested in regions far away from it, specifically in the mass regions of J/Ψ.

Chapter 4

Momentum Calibration

One of the most necessary stages of the analysis is the momentum calibration. A common technique is to make use of the known mass of some particles, for example J/ψ or Z. The momentum scale of the reconstructed tracks is calibrated or corrected so that the peak position of the invariant mass distribution reconstructed from two tracks becomes the world average value of J/ψ or Z, i.e. by the particle data group (PDG). In this thesis we will perform the energy/momentum calibration on the J/ψ and for this reason some details about the J/Ψ meson will be given.

4.1 The J/Ψ meson

The J/ψ meson [10] is the first discovered bound state of a charm quark and a charm antiquark $c\bar{c}$ (charmonium) in November 1974, in the so-called "November Revolution" of particle physics, simultaneously at Brookhaven National Laboratory and Stanford Linear Accelerator Centre (SLAC). J/ψ is special because it established the quark model as a credible description of nature. The quark model was proposed to solve certain problems of the parton model. In any way, a common feature of both models is the composite nature of hadrons. In their initial proposal, Zweig and Gell-Mann required three quarks, the up (u), down (d), and strange (s) quarks, which, despite extensive efforts to locate them in the laboratory, were not observed. The next step, therefore, was to make the appropriate combinations between the three quarks and anti-quarks to form the known hadrons and later to establish the identification of the particles from the initial experimental data with the quarks of the newer theoretical investigations, which revealed some fundamental problems. These problems were resolved by introducing an additional quantum number, called color. However, the problem of the lack of symmetry between hadrons and leptons remained - three

quarks (u, d, s) and four leptons (e^-, v_e, μ^-, v_μ). Wanting to maintain the symmetry between hadrons and leptons, Glashow and Bjorken in 1964 proposed the existence of a fourth quark, which they called charm. The introduction, however, of the fourth quark was imposed in 1970 when Glashow, Iliopoulos and Maiani proposed a mechanism named after them (G.I.M. mechanism), which fully explains the physical phenomena if we accept the existence of the fourth quark, c. Certainly, there were many questions about these particles and, therefore, until 1974 few believers accepted charm. J/ψ was the key. In November 1974, the great discovery took place. In the first experiment, carried out at Brookhaven National Laboratory (B.N.L.), Professor Ting's team from M.I.T. studied e^+e^- pairs, with a pair spectrograph, produced during the reaction:

$$p^+ \rightarrow e^+ + e^- + X$$

where X is anything, and in the e^+e^- system an unusual fine resonance at an energy of 3.1 GeV was observed. This resonance showed the production of a new particle, which they named J, and which subsequently decayed into e^+ and e^-. The same particle was detected at the Stanford Linear Collider, in the collision of positron electrons, in a collaboration between SLAC and LBL (Lawrence Berkeley Laboratory). This particle was named ψ. So its official name today is J/ψ. The resonance maximum, which was too large, was better measured in the second experiment. It was detected at an energy at the center of mass of 3.095 GeV by measuring the cross sections:

$$\sigma(e^+, e^- \rightarrow anything)$$

$$\sigma(e^+, e^- \rightarrow e^+, e^-)$$

$$\sigma(e^+, e^- \rightarrow \mu^+, \mu^-)$$

However, its amplitude could not be measured directly because it was smaller than the experimental resolution of 2MeV, but it could be examined indirectly from the experimental data, where it was found to be:

$$\Gamma_{tot} = 69 \pm 15 keV$$

The fact that the range is very narrow shows us that, despite its large mass, J/ψ is relatively long-lived. That is, it has extraordinary stability. The existence of J/ψ was therefore attributed to the existence of a new quantum number, the charm. This, in turn, led to the discovery of the charm quark, for which the pioneers of the experiments were awarded the Physics Nobel prize in 1976.

An interesting story regarding the J/ψ meson is how it got its name. Due to being discovered almost simultaneously by two different experiments, it is the only particle that has a name consisting of two letters. Richter named it "SP", after the SPEAR accelerator used at

SLAC. However, none of his coworkers liked that name. After consulting with Greek-born Leo Resvanis to see which Greek letters were still available, and rejecting "iota" because its name implies insignificance, Richter chose "psi" – a name which contains the original name "SP", but in reverse order. Ting assigned the name "J" to it, which is one letter away from "K", the name of the already-known strange meson. Another reason is that "j" is the symbol for electromagnetic current. Possibly by coincidence, "J" strongly resembles the Chinese character for Ting's name and also is the first letter of Ting's eldest daughter's name, Jeanne.

The world average value for the mass of the J/ψ meson is 3096.9 ± 0.006 MeV with a very narrow decay width 92.6 ± 1.7 keV.
In proton–proton collisions at the LHC, the J/ψ mesons can be produced through two mechanisms: the *prompt production* where the J/ψ meson is produced directly in the primary interaction and the *non-prompt production* where the J/ψ is produced in the decays from the b hadrons. The dominant J/ψ decay channel is into hadrons, while the branching ratio for lepton decays into electron–positron or muon–anti-muon pair is 5.97%.
Since electron and muon decays can be reconstructed with high purity, the J/ψ is used for calibration purposes to directly study the detector effects.

Chapter 5

Z boson mass Fit

5.1 General knowledge about the fit procedure

Fitting is the process which is used to estimate parameters of a hypothetical distribution from the observed data distribution. The most widely used method of fitting parametric models to experimental data is the method of least squares. Given a set of measurements $\{x_i, y_i \pm e_i\}$ and a model $y = f(x; \vec{\theta})$, we have the statistic χ^2:

$$\chi^2(\vec{\theta}) = \sum_{i=1}^{N} \left(\frac{y_i - f(x_i|\vec{\theta})}{e_i} \right)^2$$

Practically, the fit is done by minimizing the least-square or likelihood function.

Many difficulties in different fields of research can arise in finding the smallest value taken on by a function of one or more variable parameters. However, the classic example which occurs so often in scientific research, as in our case, is the estimation of unknown parameters in a theory by minimizing the difference, χ^2, between theory and experimental data. A direct solution exists only in the case of linear fitting, such as fitting polynomials, which is found automatically. Otherwise an iterative algorithm is used and specifically Minuit is the minimization algorithm used by default. Methods like Minuit are based on gradient and for this reason they can get easily stuck in local minima. So, it is quite common for fits to converge to a wrong solution, precisely because it is the case of a local minimum and not a global one. This is usually solved with better initial parameter values.The RooFit library of ROOT is used for the fit procedure, in which methods like Minuit are used. [11], [12]

Frequently when one wants to give a measure of how well a given null hypothesis H_o is suitable with the observed data without specific reference to any alternative hypothesis, the goodness-of-fit tests are used. The goodness-of-fit tests which were applied in this thesis are [13],[14],[15]:

1. $\frac{\chi^2}{\mathbf{ndf}}$

   It is known that if the errors of y follow a gaussian distribution then the statistic test χ^2 follows the χ^2 distribution with the number of degrees of freedom, ndf, as a parameter. Moreover, it is calculated that the expectation value of a random variable x from the χ^2 distribution is equal to the number of degrees of freedom, i.e. $E[x] = ndof$. For this reason, the χ^2 divided by the number of degrees of freedom, which is the number of bins minus the number of independent parameters, is a measure of goodness-of-fit. If it is near to one, then all is as expected. If it is much less than one, then the fit is better than expected given the size of measurement errors. This is not bad in the sense of providing evidence against the hypothesis, but it is usually a reason to check if the errors have not been overestimated or are not correlated. If it is much larger than one, there is some reason to doubt the hypothesis.

2. **Pearson's χ^2 test**

   If the errors of y follow a gaussian distribution then the statistic test χ^2 follows the χ^2 distribution with the number of degrees of freedom, ndf, as a parameter:

$$f(\chi^2, ndf) = \frac{1}{2^{ndf/2}\Gamma\left(ndf/2\right)} \left(\chi^2\right)^{\frac{ndf}{2}-1} e^{-\frac{\chi^2}{2}}$$

   with the gamma function, $\Gamma(x)$, being defined as follows:

$$\Gamma(t) = \int_0^\infty x^{t-1} e^{-x}\, dx$$

   Having found the value χ^2_{min} through the method of least square, the p-value can be found as follows:

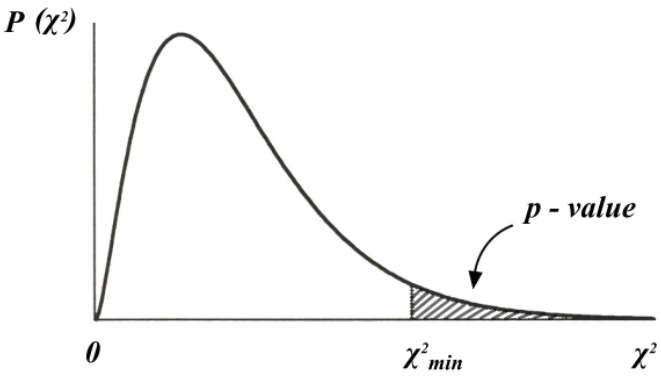

$$p - value = \int_{\chi^2_{min}}^{\infty} f(\chi^2|ndf)\, d\chi^2$$

Figure 5.1: Definition of p-value

If the fitting function is compatible with the data, the p-value should be approximately 0.5. If the p-value is close to 0, i.e. very small, the fit is not good.

3. **Pull distribution** or distribution of residuals, which is given by the equation:

$$\frac{Data - Model}{error}$$

In a good fit the residuals follow a normal distribution N(0,1).

5.2 The fit procedure to the Monte Carlo data

We use the MC data to construct the histogram of the boson mass Z with the criterion $81 < m_Z < 100$. By observing the shape of the distribution and doing various tests and combinations of functions, we conclude that the option which gives the best description of the signal is the combination of a Crystal Ball and a Gaussian distribution while for the background it is a second degree Chebyshev polynomial[16]. Thus we obtain the following result:

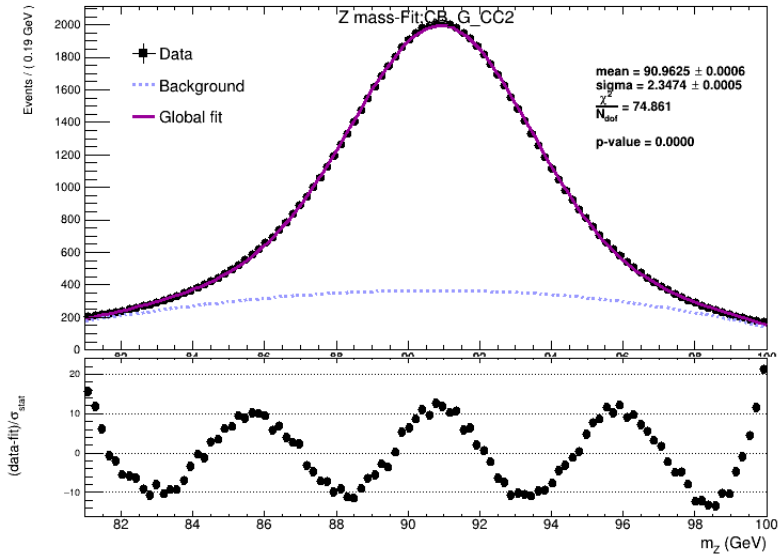

Figure 5.2: Fit to the Z boson mass without any η restriction, using MC data

We notice that although visually the fit appears good, the goodness-of-fit tests indicate the opposite. So, it indicates an improvement. Knowing that the detector does not have the same resolution in all its parts, it was decided to divide the detector into 11 η regions for the range $[-1.1, 1.1]$.

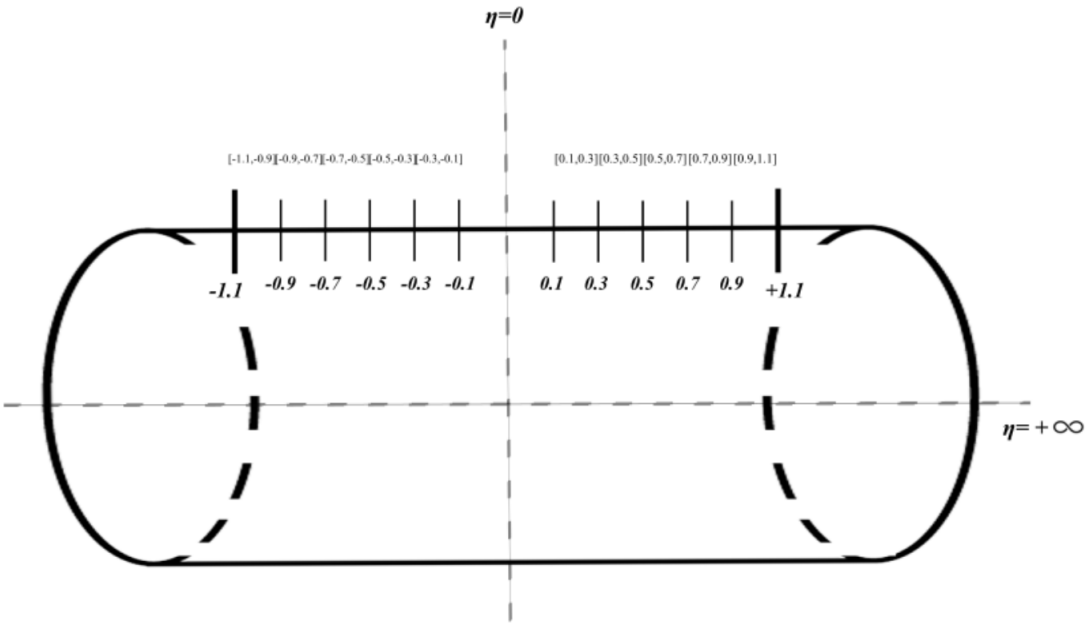

Figure 5.3: Separation of the detector into η-regions

Hence, because each of the two muons can be detected in one of these η regions, 11×11 mass histograms and the corresponding fits are created. The improvement is obvious, not only visually but also from the goodnes-of-fit tests. An indicatory example is given as follows:

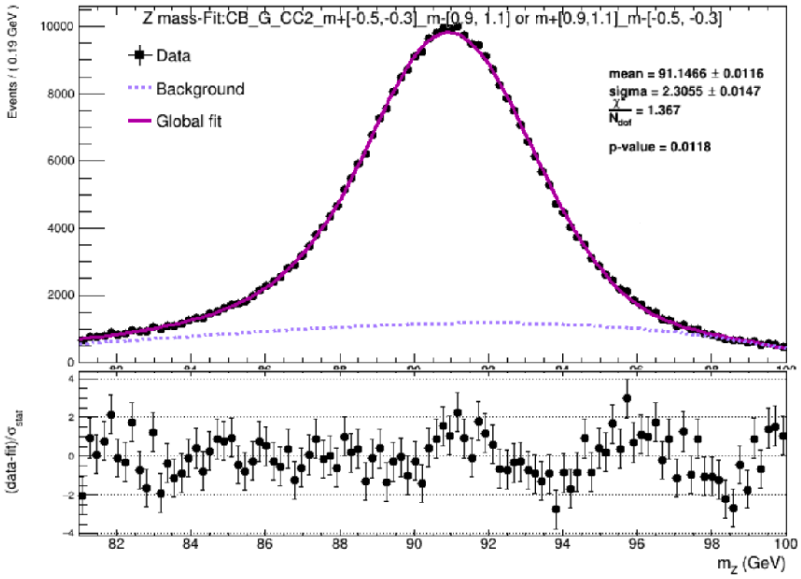

Figure 5.4: Fit of Z boson mass for η regions (-0.5,-0.3)(0.9,1.1)

It is observed that there are events in all possible combinations of η regions of the two muons, which means that the muons from the decay of the Z boson can be produced at a large angle to each other. Going a little deeper, we want to examine the dependence of the number of events as a function of the η regions of the two muons. Thus we have the following graph:

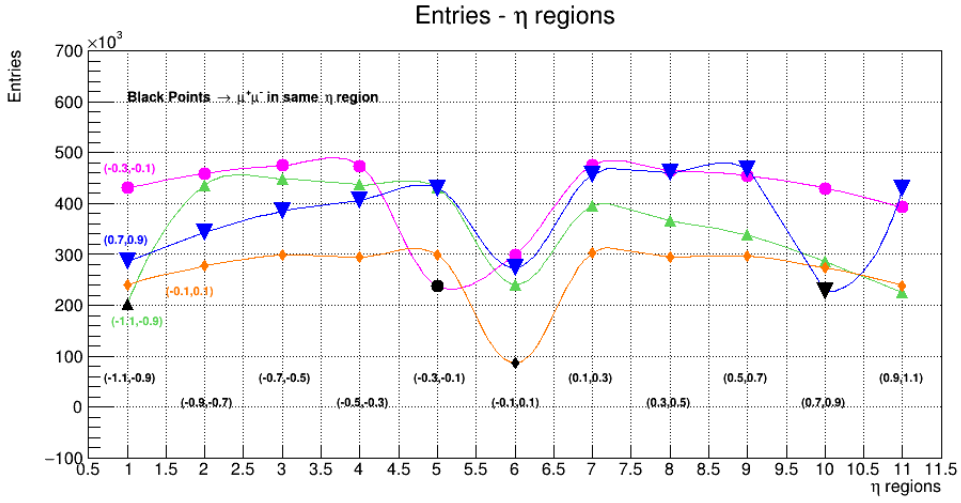

Figure 5.5: Entries per specific η regions of two muons from Z decay. Practically we select a reference η region each time and we make all possible combinations with all the η regions. Indicatively, we draw some of these combinations so that the graph is distinct and can be analyzed. Each reference region is drawn in a different colour, while the η regions are marked in black

From the graph, Fig.5.5, by studying each curve separately, we arrive at some common observations. Firstly, the fewest entries, which can be used for statistical analysis, are observed when the two muons are produced in the same η region. When the muons are in adjacent η regions, most events are observed and when the angle between them is increased, there is a gradual small decrease in the number of entries. Looking now at the graph as a whole, some curves are more elevated than others. For this reason, if we want to explore a little more the relevance of the entries to the η region, we create an histogram of muons' pseudorapidity η.

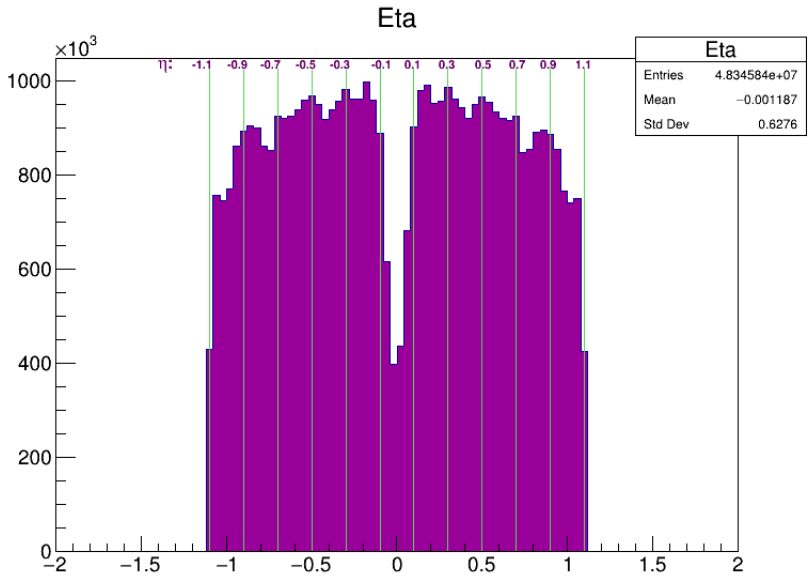

Figure 5.6: Histogram of η

As we expect, the Fig.5.6 confirms that our detector is not perfect. In some η regions it has better resolution while in others it has worse, which may be due to various reasons such as dead zones. If we compare the histograms Fig.5.5 and Fig.5.6, we observe that the curves that are more elevated, namely the blue and magenta ones, correspond to the regions with the most events, i.e., the regions (0.7,0.9) and (-0.3,-0.1) respectively. Furthermore, with a more general look at the histogram Fig.5.6, we have a higher statistic in the central regions of the barrel compared to its outer regions.

After, we draw two graphs with the mass and standard deviation (σ) fitted found parameters. Practically, in order to examine the values of the mass parameter in relation to the η regions where the muons are detected, each time we assume that one of the two muons is found in a η region and the other one scans all η regions so that all possible combinations are made. The same procedure is repeated for all η regions. To make this methodology easier

to understand, a schema is provided as follows:

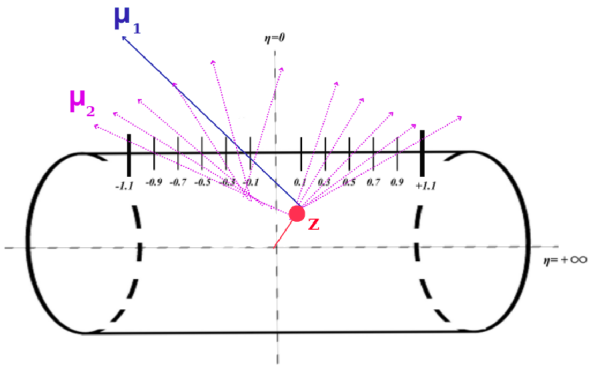

Figure 5.7: Schematically the followed methodology of analysis

Thus, the following graphs are obtained:

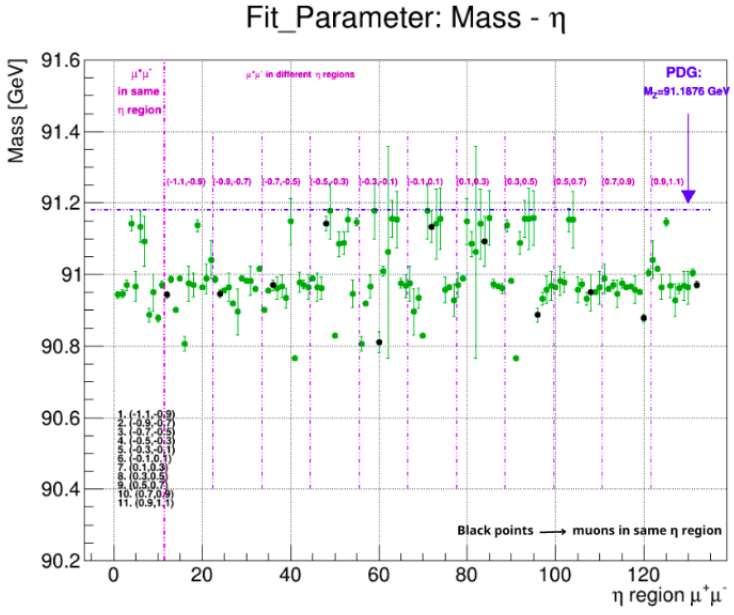

Figure 5.8: Fitted parameter of mass. The η regions colored in magenta refer to μ_1

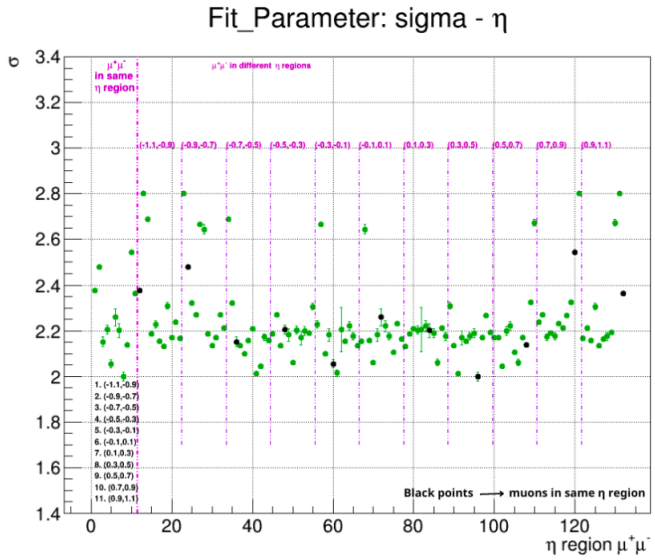

Figure 5.9: Fitted parameter of standard deviation, σ. The η regions colored in magenta refer to μ_1

At first glance, we notice that there is a variation in the fitted parameter, both in the mass and in the standard deviation (σ) parameter. However, it is more intense for σ. As far as Fig.5.8 is concerned, we observe a variation of the fitted parameter of mass. Focusing on the first part, i.e. the case when both muons are produced in the same η region, we observe that in the central regions of the barrel we obtain better values. As to the second part of the graph, i.e. when the muons are produced in different η regions there is a variation which is more visible in the central regions of the detector; i.e. we observe a better measurement of the mass parameter. If we examine the causes of this variation we should reject the scenario of a sole statistical error because comparing the histogram of the pseudorapidity distribution η, Fig.5.6, with the graph Fig.5.8, we should have better results in other η regions such as (0.5,0.7). Moreover, as it was proved before, the muons from the decay of Z, between the region [-1.1,1.1], can be produced with big angles between them, and as shown in Fig.5.5, this does not affect the statistics significantly. Therefore, this variation reveals a systematic error which could be due to a bad reconstruction when muons are produced in the edges of the barrel, i.e. when they are produced at bigger angles.

5.3 The fit procedure to the Data

After we have found that the model 1 Crystal Ball + 1 Gauss + 1 Chebysev describes the boson Z mass in the MC data satisfactorily, we apply it to the data to examine if similar

results are obtained. Therefore, we follow exactly the same procedure with the MC data, starting with the fit to the data without any η restriction.

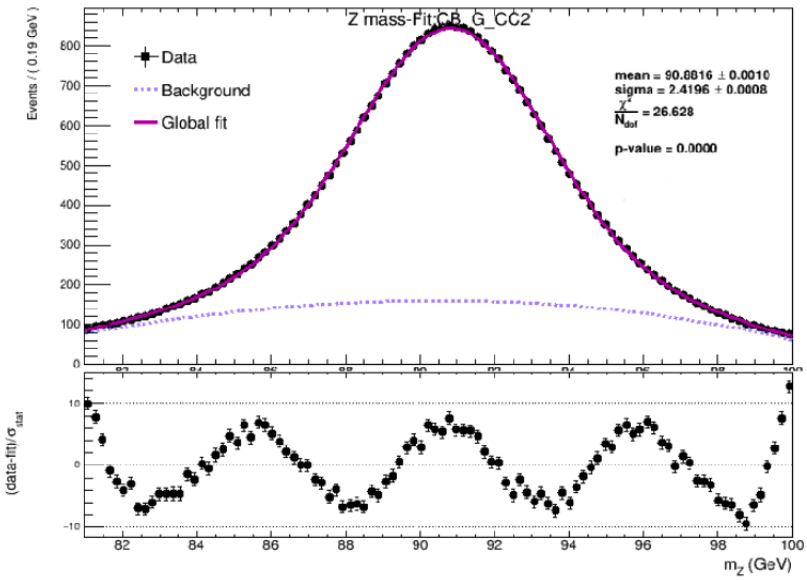

Figure 5.10: Fit to the Z boson mass without any η restriction

As expected from the fit procedure to the MC data, the fit is not successful. So we separate the data into η regions, where we obtain 11×11 fits. Indicatively, the following fit is provided as an example:

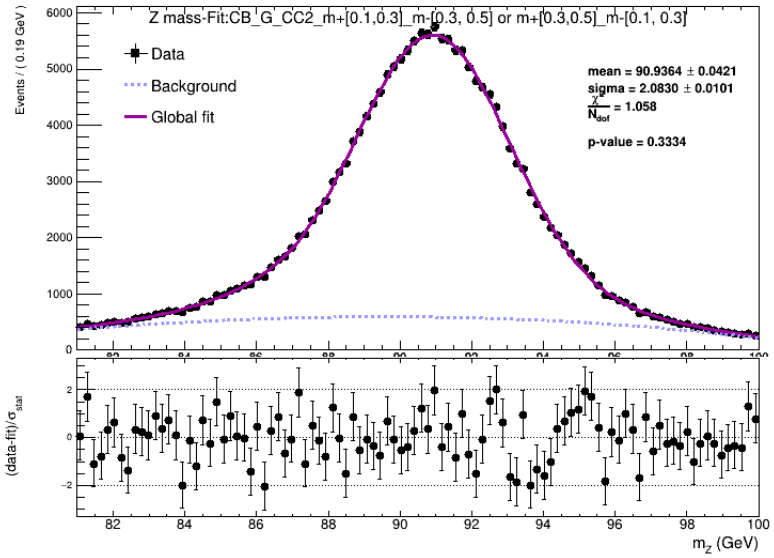

Figure 5.11: Fit to the Z boson mass for η: (0.1,0.3)(0.3,0.5)

It is obvious that the fit to the data, after separating the detector into η regions, presents a significative improvement.

If we examine now the dependence of the entries per combination of η regions of the two muons, we have the following graph:

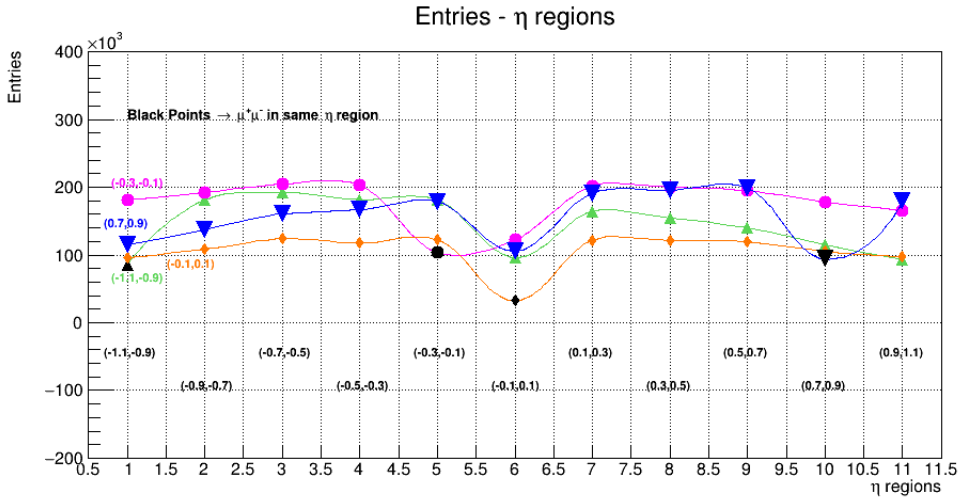

Figure 5.12: Entries per specific η regions of two muons. Practically we select a reference η region each time and make all possible combinations with all the η regions. Indicatively, we draw some of these combinations so that the graph is distinct and can be analyzed. Each reference region is drawn in a different colour, while the η regions are marked in black

We observe that we have the same image as to the MC data, i.e. in each curve there

is a minimum, the point in black, which characterizes the case in which the two muons are detected in the same η region. Thus, in this case we have the fewest events. In the case where the two muons are detected in adjacent η regions most of the events are recorded, while as the η distance of the muons increases, the events gradually decrease. In total, there is again this elevation of some curves due to the fact that the detector is not detecting with the same resolution in all places, as shown in the histogram below:

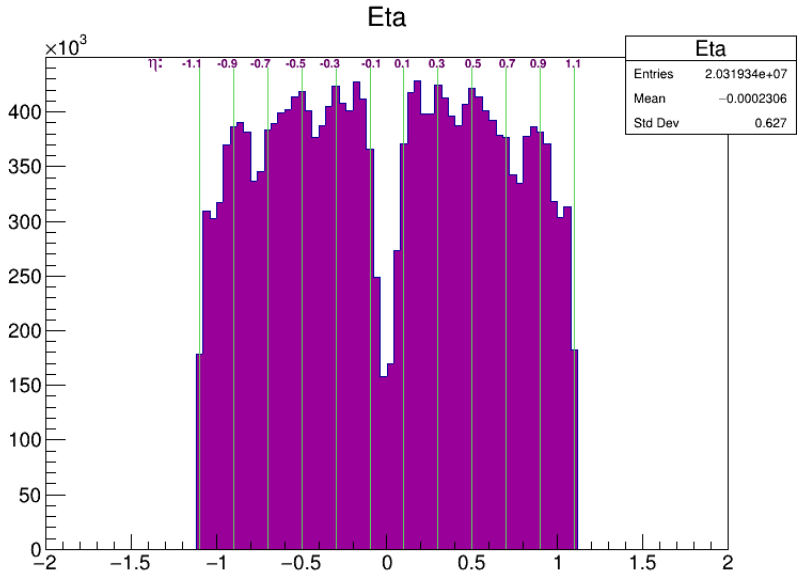

Figure 5.13: Histogram of muons' η for $-1.1 < \eta < 1.1$

After, we make the two graphs with the fitted parameters, i.e. mass and sigma:

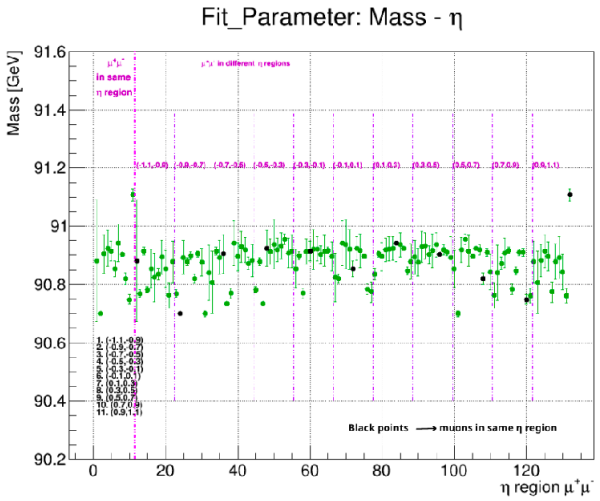

Figure 5.14: Fitted parameter: Mass of boson Z. The η regions colored with magenta refer to μ_1

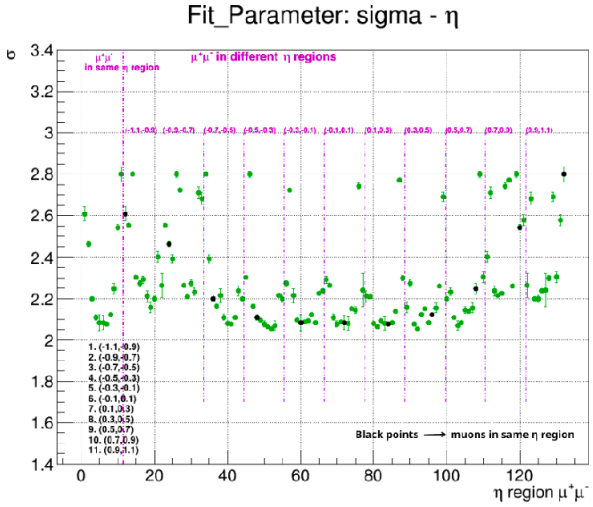

Figure 5.15: Fitted parameter: σ. The η regions colored with magenta refer to μ_1

In a general view, we observe that in the data there is also a variation in the parameters depending on the η region, in which each muon is produced, with the most significant variation being that of the σ. However, the illustration of Fig.5.14 is not the same as that of the MC data, Fig. 5.8, because although a slight elevation of the values in the central regions of the barrel is observed, it is not as significant as that of the MC data, where a systematic error is clearly revealed. This logically suggests that some corrections need to be made to the MC.

Chapter 6

Precision measurement of boson Z mass

One of the many goals of the ATLAS experiment is to measure with precision the mass of the boson Z. This need comes from the fact that most of the energy/momentum calibrations in ATLAS rely on the mass of Z, for example m_W/m_Z and m_H/m_Z. The value of the Z mass, which is still used today, was measured by LEP in 1993 to be $M_Z = (91.187 \pm 0.0021)$ GeV. Therefore, it is necessary to measure it again by the LHC as better statistics has been achieved and its detectors have been improved structurally. Recently the CDF II experiment provided a new measurement of the Z mass, which is $m_Z = 91.192 \pm 6.4$ stat. ± 4.0 sys. MeV [17].

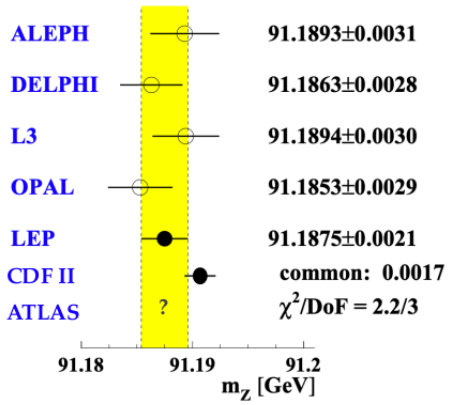

Figure 6.1: Measurements of the boson Z mass value

In regard to the LEP experiment, its largest source of uncertainty is the energy calibration of the beam. For this reason special attention will be given to the energy/mo-

mentum calibration. In particular, for a precise measurement of the boson mass Z, i.e. $dm_Z = 10^{-5}$, we need to perform the energy/momentum calibration on the J/ψ in order to achieve $dm_{J/\psi} = 10^{-6}$.

6.1 Armenteros-Podolanski plot

A new method for calibrating the momentum scale in a particle physics detector will be now described. The Armenteros-Podolanski plot is a representation of the transverse momentum of a two-body decay versus the asymmetry of the longitudinal momentum, α, of the decay products

$$\alpha = \frac{p_{1l} - p_{2l}}{P} \tag{6.1}$$

In this space, two-body decays appear as semi-ellipses, whose parameters provide information on the masses of the parent and the child particles. The method relies on the determination of the masses of the final state particles in two-body decays of neutral particles, which can then be used to obtain corrections in the momentum scale. By fitting the ellipses, one can retrieve the masses of the parent and the child particles. Deviations from known values then give useful information about detector and reconstruction effects.
At present, the calibration of the momentum scale of LHC detectors uses the fit of the invariant mass of known resonances, such as $J/\psi \to \mu^+\mu^-$ decays. The precision of this method is ultimately limited by the knowledge of such masses. Our objective is to demonstrate that the Armenteros-Podolanski plot allows a significantly more precise momentum scale calibration than using only parent particles, as long as child particle masses are better known that parent ones. The key advantage of our proposed method is that it uses the precisely known masses of the final state particles of the decay (e.g, pions, protons, muons...) to calibrate the momentum scale of the detector, instead of the less precisely measured masses of the heavier parent particles.

This representation was proposed in 1954 by R. Armenteros and J. Podolanski as a method of analysis of the dynamics of neutral particles decaying to two bodies (V^0 particles). The need for such a method was felt after the inhomogeneity of neutral V-particles had been discovered by the Pic du Midi group. [18],[19]

6.2 Equations

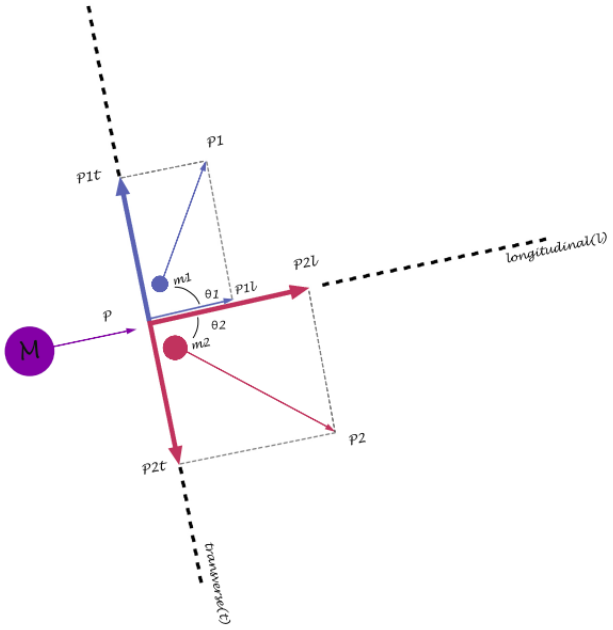

Figure 6.2: Kinematics of a two-body decay in the laboratory (LAB)

Analysing the Fig. 6.2, the following equations are obtained [20]:

$$\overrightarrow{P_1} = \overrightarrow{P_{1t}} + \overrightarrow{P_{1l}} \tag{6.2}$$

$$\overrightarrow{P_2} = \overrightarrow{P_{2t}} + \overrightarrow{P_{2l}} \tag{6.3}$$

From the conservation of momentum, we have that the total momentum in the transverse plane is $\Delta\overrightarrow{P_t} = 0$ and so:

$$\overrightarrow{P_{1t}} = -\overrightarrow{P_{2t}} \rightarrow P_{1t} = P_{2t} = P_t \tag{6.4}$$

We, also, have that:

$$\overrightarrow{P} = \overrightarrow{P_1} + \overrightarrow{P_2} \xLeftrightarrow{(6.2),(6.3)} \overrightarrow{P} = \overrightarrow{P_{1l}} + \overrightarrow{P_{1t}} + \overrightarrow{P_{2l}} + \overrightarrow{P_{2t}} \xLeftrightarrow{(6.4)} \overrightarrow{P} = \overrightarrow{P_{1l}} + \overrightarrow{P_{2l}} \tag{6.5}$$

and

$$P = P_{1l} + P_{2l} \tag{6.6}$$

Using the relation (6.6) we obtain that:

$$P_{2l} = P - P_{1l} \tag{6.7}$$

and thus, the equation (6.1) becomes:

$$a = \frac{P_{1l} - P + P_{1l}}{P} \Leftrightarrow a = \frac{2P_{1l} - P}{P} \Leftrightarrow P_{1l} = \frac{1+a}{2}P \tag{6.8}$$

Inserting (6.8) into (6.7), we have:

$$P_{2l} = P - \frac{1+a}{2}P \Leftrightarrow P_{2l} = \frac{1-a}{2}P \tag{6.9}$$

Continuing,

$$P_1^2 = P_{1l}^2 + P_{1t}^2 \Leftrightarrow P_1^2 \overset{(6.8)}{=} \left(\frac{1+a}{2}P\right)^2 + P_t^2 \Leftrightarrow P_1^2 = \frac{(1+a)^2}{4}P^2 + P_t^2 \tag{6.10}$$

and respectively for particle 2:

$$P_2^2 = P_{2l}^2 + P_{2t}^2 \overset{(6.9)}{\Longleftrightarrow} P_2^2 = \frac{(1-a)^2}{4}P^2 + P_t^2 \tag{6.11}$$

Now, we want to calculate the quantity $\overrightarrow{P_1}\overrightarrow{P_2}$:

$$\begin{aligned}
&\overrightarrow{P_1}\overrightarrow{P_2} = (\overrightarrow{P_{1l}} + \overrightarrow{P_{1t}})(\overrightarrow{P_{2l}} + \overrightarrow{P_{2t}}) = \overrightarrow{P_{1l}}\overrightarrow{P_{2l}} + \overrightarrow{P_{1l}}\overrightarrow{P_{2t}} + \overrightarrow{P_{1t}}\overrightarrow{P_{2l}} + \overrightarrow{P_{1t}}\overrightarrow{P_{2t}} \overset{(6.4)}{=} \overrightarrow{P_{1l}}\overrightarrow{P_{2l}} + \overrightarrow{P_{1t}}(-\overrightarrow{P_{2t}}) \Leftrightarrow \\
&\overrightarrow{P_1}\overrightarrow{P_2} = \left(\frac{1+a}{2}\right)\left(\frac{1-a}{2}\right)P^2 - P_t^2 \Leftrightarrow \frac{(1+a)(1-a)}{4}P^2 - P_t^2 \Leftrightarrow \overrightarrow{P_1}\overrightarrow{P_2} = \frac{1-a^2}{4}P^2 - P_t^2
\end{aligned} \tag{6.12}$$

The four-vectors that describe particles with momenta $\overrightarrow{P_1}$ and $\overrightarrow{P_2}$ are $P_1^\mu = (E_1, \overrightarrow{P_1})$ and $P_2^\mu = (E_2, \overrightarrow{P_2})$, where $E_1^2 = \sqrt{P_1^2 + m_1^2}$ and $E_2^2 = \sqrt{P_2^2 + m_2^2}$.

A quantity which is conserved in the system of the decay of the particle M into two particles m_1 and m_2 is $P^\mu = P_1^\mu + P_2^\mu = (E_1 + E_2, \overrightarrow{P_1} + \overrightarrow{P_2})$, for which:

$$|P^\mu|^2 = P^\mu P_\mu = (E_1 + E_2)^2 - (\overrightarrow{P_1} + \overrightarrow{P_2})^2 = E^2 + P^2 = M^2 \tag{6.13}$$

So, from the equation (6.13) we have that:

$$\begin{aligned}
&M^2 = (E_1 + E_2)^2 - (\overrightarrow{P_1} + \overrightarrow{P_2})^2 M^2 \Leftrightarrow \\
&\Leftrightarrow M^2 = m_1^2 + m_2^2 + 2\sqrt{P_1^2 + m_1^2}\sqrt{P_2^2 + m_2^2} - 2\overrightarrow{P_1}\overrightarrow{P_2} \Leftrightarrow \\
&\Leftrightarrow 2\sqrt{P_1^2 + m_1^2}\sqrt{P_2^2 + m_2^2} = M^2 - m_1^2 - m_2^2 + 2\overrightarrow{P_1}\overrightarrow{P_2} \Leftrightarrow \\
&\Leftrightarrow 4(P_1^2 + m_1^2)(P_2^2 + m_2^2) = (M^2 - m_1^2 - m_2^2 + \overrightarrow{P_1}\overrightarrow{P_2})^2 \Leftrightarrow \\
&\Leftrightarrow 4\left(P_1^2 P_2^2 + P_1^2 m_2^2 + m_1^2 P_2^2 + m_1^2 m_2^2\right) = \left(M^2 - m_1^2 - m_2^2 + 2\overrightarrow{P_1}\overrightarrow{P_2}\right)^2
\end{aligned} \tag{6.14}$$

Analytically some terms of the equation (6.14):

$$\triangleright\ \overrightarrow{P_1}^2\overrightarrow{P_2}^2 \overset{(6.10),(6.11)}{=} \left(\frac{(1+a)^2}{4}P^2 + P_t^2\right)\left(\frac{(1-a)^2}{4}P^2 + P_t^2\right) \overset{op.}{=} \frac{(1-a^2)^2}{16}P^4 + \frac{a^2+1}{2}P^2P_t + P_t^4 \tag{6.15a}$$

$$\triangleright\ m_2^2P_1^2 \overset{(6.10)}{=} m_2^2\frac{(1+a)^2}{4}P^2 + m_2^2P_t^2 \tag{6.15b}$$

$$\triangleright\ m_1^2P_2^2 \overset{(6.11)}{=} m_1^2\frac{(1-a)^2}{4}P^2 + m_1^2P_t^2 \tag{6.15c}$$

Hence, inserting (6.12), (6.15) into (6.14) and setting that:

$$\delta' = M^2 - m_1^2 - m_2^2 + \frac{1-a^2}{2}P^2$$

(operations are facilitated), we obtain:

$$P_t^2 = \frac{\frac{\delta'}{4} - \frac{(1-a^2)P^4}{16} - \frac{P^2[m_2^2(1+a^2)^2 + m_1^2(1-a)^2]}{4} - m_1^2m_2^2}{m_1^2 + m_2^2 + \frac{P^2(1+a^2)}{2} + 2\delta'}$$

and setting again that $\delta^2 = \frac{\delta'^2}{4}$ the above equation can be written:

$$P_T^2 = \frac{\delta^2 - \frac{(1-a^2)P^4}{16} - \frac{P^2[m_2^2(1+a)^2 + m_1^2(1-a)^2)]}{4} - m_1^2m_2^2}{m_1^2 + m_2^2 + \frac{P^2(1+a^2)}{2} + 2\delta} \tag{6.16}$$

If we assume that N and D are the numerator and denominator of the above expression(6.16), then we have for the denominator:

$$\left.\begin{aligned} D &= m_1^2 + m_2^2 + \frac{P^2(1+a^2)}{2} + 2\delta \\ \delta &= \frac{\delta'}{2} = \frac{1}{2}(M^2 - m_1^2 - m_2^2 + \frac{1-a^2}{2}P^2) \end{aligned}\right\} \Leftrightarrow D = M^2 + P^2 \tag{6.17}$$

while for the numerator N,using the fact that:

$$\delta^2 - \frac{(1-a^2)^2P^4}{16} =$$

$$\left(\delta - \frac{1-a^2}{4}P^2\right)\left(\delta + \frac{1-a^2}{4}P^2\right) =$$

$$\left(\frac{M^2 - m_1^2 - m_2^2}{2}\right)\left(\frac{M^2 - m_1^2 - m_2^2}{2} + \frac{1-a^2}{2}P^2\right)$$

it can be written as:

$$N = \frac{(M^2 - m_1^2 - m_2^2)^2}{4} + \frac{P^2(1-a^2M^2)}{4} - \frac{P^2[m_1^2(1-a) + m_2^2(1+a)]}{2} - m_1^2m_2^2 \tag{6.18}$$

Thus, the equation (6.16) due to (6.17),(6.18) takes the form:

$$\boxed{p_t = \sqrt{\frac{\frac{(M^2-m_1^2-m_2^2)^2}{4} + \frac{P^2(1-a^2)M^2}{4} - \frac{P^2[m_1^2(1-a)+m_2^2(1+a)]}{2} - m_1^2 m_2^2}{P^2+M^2}}} \tag{6.19}$$

Note that for big momentum, $P >> M$, the p_t is independent of the momentum P of the incident particle of mass M and thus:

$$\boxed{p_t = \sqrt{\frac{(1-a^2)}{4}M^2 - \frac{m_1^2(1-a)+m_2^2(1+a)}{2}}} \tag{6.20}$$

6.3 Conception

Initially, an attempt will be made to understand the equation (6.20). For this reason, the first task we need to do is to create the Armenteros-Podolanski plots for both J/ψ and Z, as we want to examine the behavior of the relation (6.20) at small and large masses. Therefore, we have:

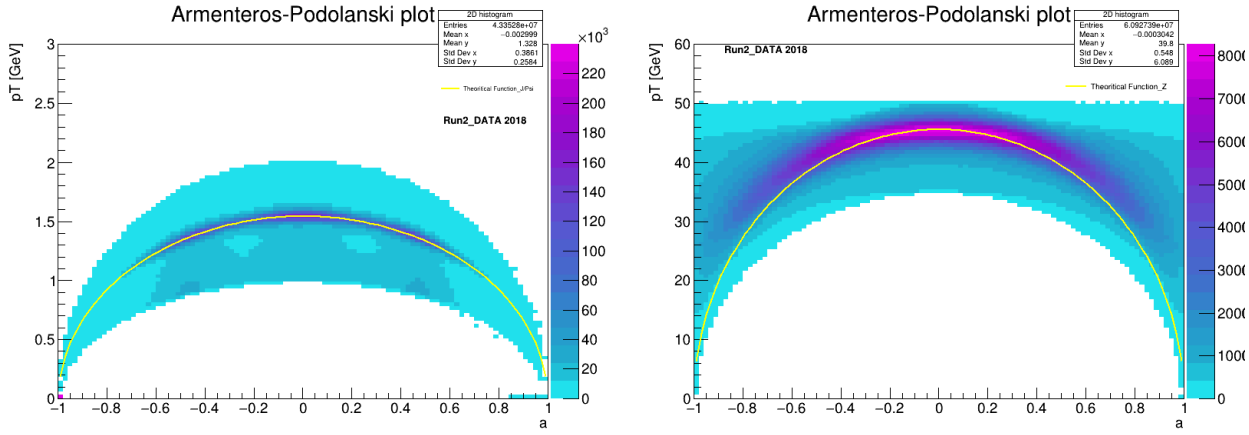

(a) JPsi **(b)** Z

Figure 6.3: Armenteros-Podolanski plot

It is observed that the semi-ellipse fully satisfies the J/Ψ data but not the Z data, mainly at the extreme values of $a, (a \to 1)$. This result was expected as the relation (6.20) is used for $P >> M$, which is not the case of Z since, as it can be seen from the Fig.6.7, the most data have momentum close to the mass value of Z. So, the next question that arises is whether there are momenta of Z for which the equation (6.20) is satisfied, i.e. its transverse momentum is independent of its total momentum. To answer this question, the Wolfram Mathematica program is used, where the relation (7.1) is drawn for several momenta which are multiples of Z mass:

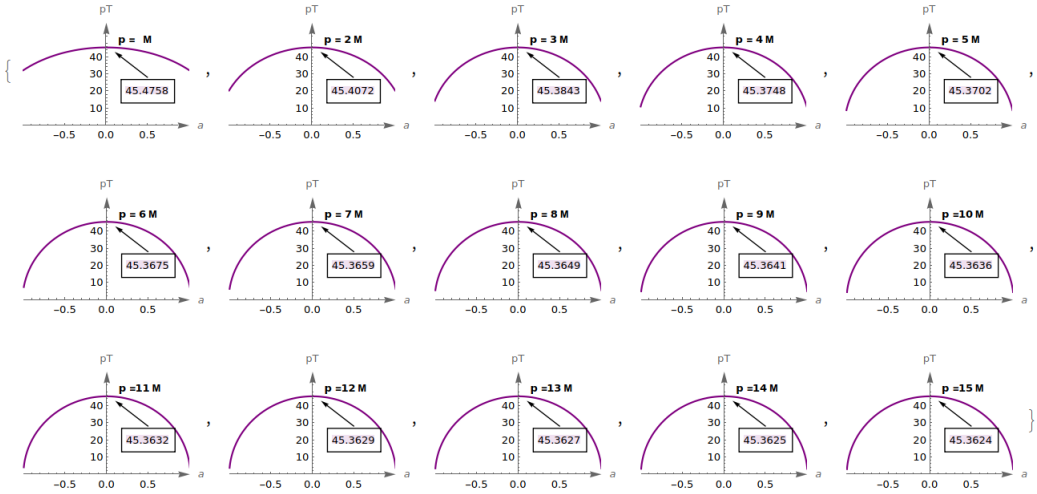

Figure 6.4: Armenteros-Podolanski plots for P multiples of Z mass using Mathematica

At a first glance at the Fig.6.4, it can be observed that for $P > 6M$, the semi-ellipses remain almost the same. To confirm this observation, the percentage change in transverse momentum is also calculated through the Mathematica, as shown in the Figure below:

	a=-1	a=-0.75	a=-0.5	a=-0.25	a=0	a=0.25	a=0.5	a=0.75	a=1
M	-41.4217	-17.9537	-6.90454	-1.60011	1.55855×10^{-14}	-1.60011	-6.90454	-17.9537	-41.4217
2 M	-58.1325	-14.3212	-4.58417	-0.982383	-1.55855×10^{-14}	-0.982383	-4.58417	-14.3212	-58.1325
3 M	-41.4357	-5.54455	-1.60067	-0.330697	0.	-0.330697	-1.60067	-5.54455	-41.4357
4 M	-30.3951	-2.43217	-0.671045	-0.13667	-1.55855×10^{-14}	-0.13667	-0.671045	-2.43217	-30.3951
5 M	-23.6788	-1.24	-0.334613	-0.0676974	0.	-0.0676974	-0.334613	-1.24	-23.6788
6 M	-19.3013	-0.708093	-0.18875	-0.0380503	1.55855×10^{-14}	-0.0380503	-0.18875	-0.708093	-19.3013
7 M	-16.2558	-0.439572	-0.116307	-0.023396	0.	-0.023396	-0.116307	-0.439572	-16.2558
8 M	-14.0256	-0.290607	-0.0765222	-0.0153718	0.	-0.0153718	-0.0765222	-0.290607	-14.0256
9 M	-12.3264	-0.201725	-0.0529432	-0.0106253	0.	-0.0106253	-0.0529432	-0.201725	-12.3264
10 M	-10.9907	-0.145559	-0.0381125	-0.00764377	0.	-0.00764377	-0.0381125	-0.145559	-10.9907

Figure 6.5: Calculations of the rate of change of transverse momentum, p_T, for different values of α and momentum P

Indeed, as shown by the calculations in Fig.6.5, for momenta $P_Z > 6M_Z$ the transverse momentum has a minimal, almost zero variation for all values of α except for $\alpha = \pm 1$ for which there is a slight modification. However, we assume that, in total, for momenta six times bigger than the mass of Z the change in transverse momentum is negligible.
All the above that have been researched, will be applied to the data. Initially, we start by examining if there are data with momentum bigger than six times their mass. For this reason, a 2D mass - momentum histogram and a histogram of momentum are made:

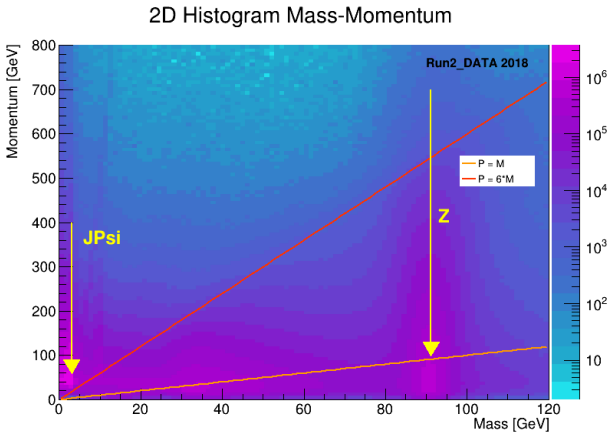

Figure 6.6: 2D Histogram $M - P$

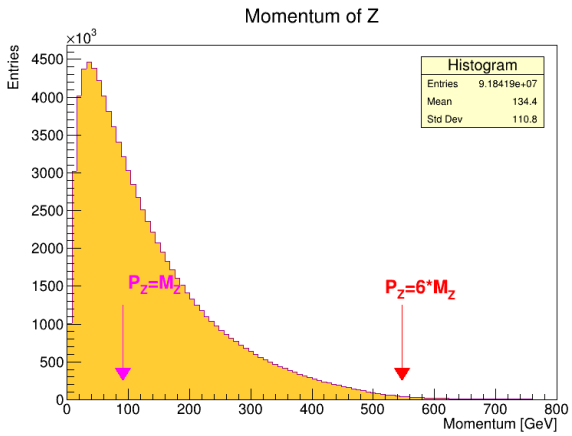

Figure 6.7: Momentum of Z

It is observed that for $P > 6M_Z$, most of the Z data are cut off.

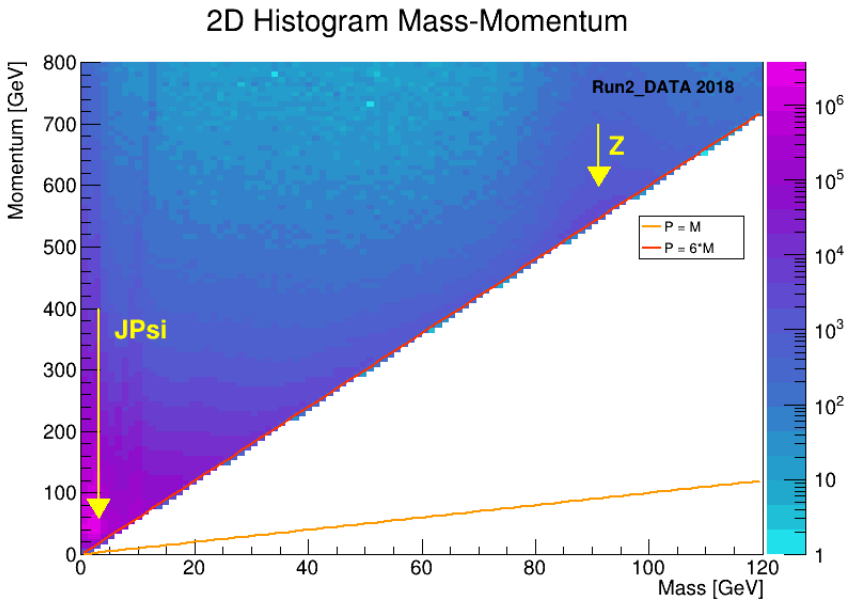

Figure 6.8: 2D Histogram M-P with criteria $P > 6M$

However, some of them remain, as shown in the Fig.6.8, which will be used to construct the Armenteros-Podolanski plot:

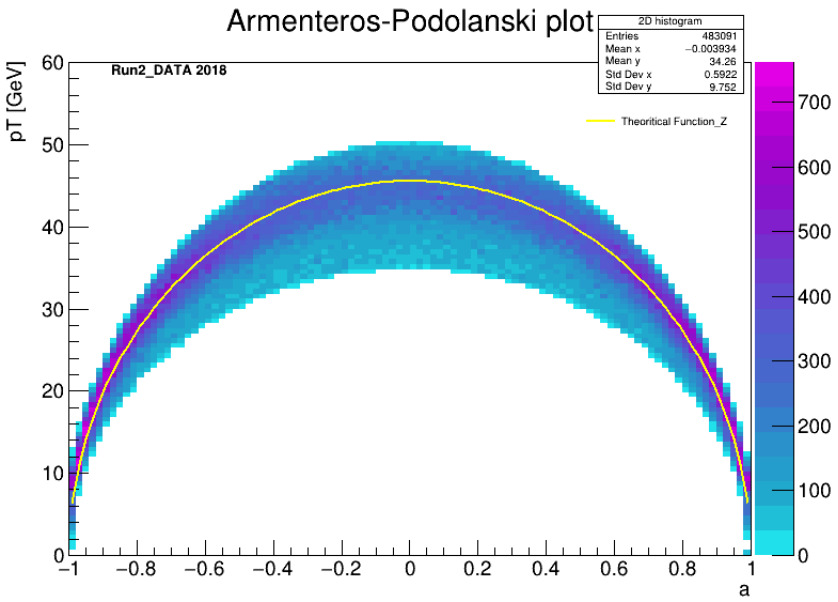

Figure 6.9: Armenteros-Podolanski plot for Z with $P > 6M$

Having applied the momentum criterion, the semi-ellipse now satisfies our Z data.

Following the same procedure for J/ψ, with the aid of Mathematica we have:

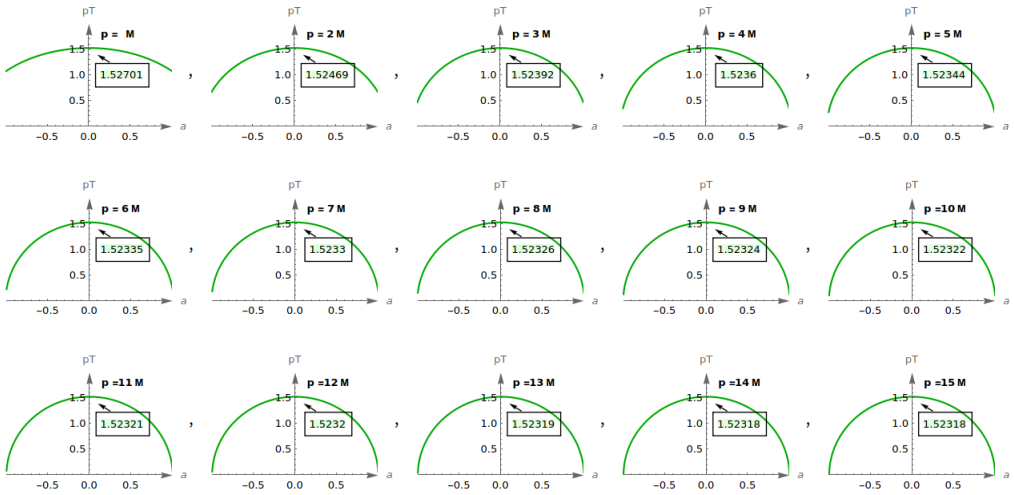

Figure 6.10: Armenteros-Podolanski plots for P multiples of J/ψ mass using Mathematica

and also:

	a=-1	a=-0.75	a=-0.5	a=-0.25	a=0	a=0.25	a=0.5	a=0.75	a=1
M	-41.7537	-18.0618	-6.94028	-1.60778	0.	-1.60778	-6.94028	-18.0618	-41.7537
2 M	-59.242	-14.4308	-4.60877	-0.98684	1.43775×10^{-14}	-0.98684	-4.60877	-14.4308	-59.242
3 M	-43.1399	-5.59404	-1.60971	-0.332218	0.	-0.332218	-1.60971	-5.59404	-43.1399
4 M	-32.6747	-2.45542	-0.674928	-0.137305	0.	-0.137305	-0.674928	-2.45542	-32.6747
5 M	-26.5876	-1.25226	-0.336574	-0.0680141	0.	-0.0680141	-0.336574	-1.25226	-26.5876
6 M	-22.934	-0.715225	-0.189864	-0.038229	0.	-0.038229	-0.189864	-0.715225	-22.934
7 M	-20.7541	-0.44405	-0.116996	-0.0235062	-1.43775×10^{-14}	-0.0235062	-0.116996	-0.44405	-20.7541
8 M	-19.6014	-0.29359	-0.0769773	-0.0154444	1.43775×10^{-14}	-0.0154444	-0.0769773	-0.29359	-19.6014
9 M	-19.3071	-0.203807	-0.0532587	-0.0106755	0.	-0.0106755	-0.0532587	-0.203807	-19.3071
10 M	-19.9136	-0.147067	-0.03834	-0.00767994	0.	-0.00767994	-0.03834	-0.147067	-19.9136

Figure 6.11: Calculations of the rate of change of transverse momentum, p_T, for different values of α and momentum P for J/Ψ

It is evident that for momenta bigger than six times the mass of J/ψ, the curve remains almost the same, which is confirmed by calculating the percentage change in transverse momentum for different momenta of the J/ψ particle. Constructing the histogram of the momentum of J/Ψ (Fig. 6.12), it is observed that almost all J/Ψ data satisfy the condition $P > 6M$.

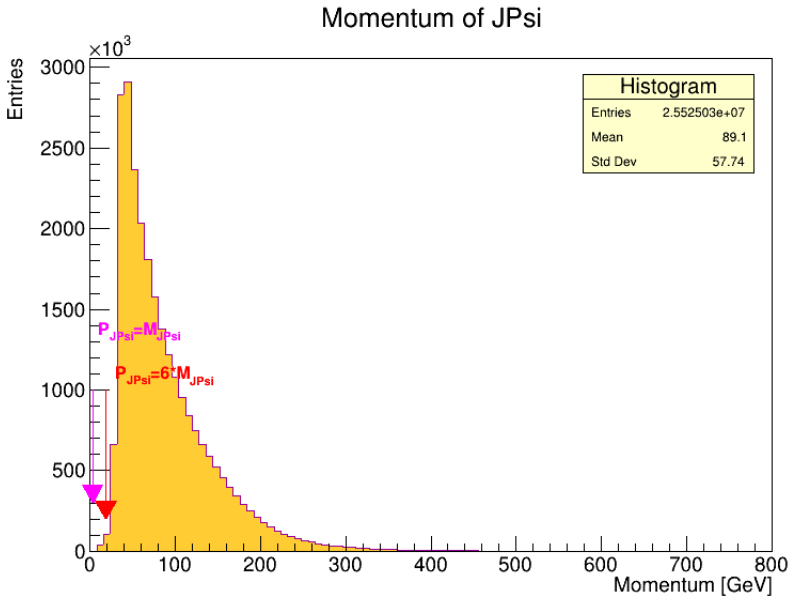

Figure 6.12: Momentum of J/Ψ

For this reason, without applying any momentum criterion to the J/ψ data, the relation (6.20) is satisfied, i.e. the Armenteros-Podolanski plots, as shown in Fig.6.3a.

Another curious point is in the Fig.6.4 and Fig.6.10 because as it can be noticed, for $\alpha = 0$, as the momentum of Z and J/ψ increases, the transverse momentum does not change but remains constant, unlike for the extreme values of α. Using the equation (7.1)

$$p_T = \sqrt{\frac{\frac{(M^2-m_1^2-m_2^2)^2}{4} + \frac{P^2(1-a^2)M^2}{4} - \frac{P^2[m_1^2(1-a)+m_2^2(1+a)]}{2} - m_1^2m_2^2}{P^2+M^2}}$$

for $a = 0$ and $m1 = m2 = m$

$$p_T = \sqrt{\frac{\frac{(M^2-2m^2)^2}{4} + \frac{P^2M^2}{4} - p^2m^2 - m^4}{P^2+M^2}} \Leftrightarrow\Leftrightarrow p_T = \sqrt{\frac{\frac{M^4-4M^2m^2+4m^4}{4} + P^2(\frac{M^2}{4} - m^2) - m^4}{P^2+M^2}}$$

$$\Leftrightarrow p_T = \sqrt{\frac{\frac{M^4}{4} - M^2m^2 + P^2(\frac{M^2}{4} - m^2)}{P^2+M^2}} \Leftrightarrow p_T = \sqrt{\frac{M^2(\frac{M^2}{4} - m^2) + P^2(\frac{M^2}{4} - m^2)}{P^2+M^2}}$$

$$\Leftrightarrow p_T = \sqrt{\frac{(\frac{M^2}{4} - m^2)(P^2+M^2)}{P^2+M^2}} \Leftrightarrow\Leftrightarrow p_T = \sqrt{M^2(\frac{1}{4} - \frac{m^2}{M^2})}$$

but $M >> m$ so the term $\frac{m^2}{M^2} \to 0$. Thus,

$$\boxed{p_T = \frac{M}{2}} \tag{6.21}$$

Therefore, we can conclude that when the two muons are produced with the same longitudinal momentum ($\alpha = 0$), then their transverse momentum depends only on the mass of the parent particle, as for example J/Ψ or Z, and in particular its value is constant and equal to:

$$p_{T_1} = p_{T_2} = \frac{M}{2}$$

which can be seen in the boxes of the Fig.6.4 and Fig.6.10. Specifically, in the Fig.6.4, which is refered to boson Z, we have that $p_{T_{max}} = \frac{M}{2} \simeq 45.6$ and respectively in the Fig.6.10, which is refered to J/Ψ, we have that $p_{T_{max}} = \frac{M}{2} \simeq 1.5$.

6.4 Fitting Test

The first and identifying test of this calibration method is to examine the value of the mass parameter ($M_{J/\Psi}$) that is found by fitting the Armenteros-Podolanski plot, using the function (6.20) and knowing from the Particle Data Group that $M_{J/\Psi} = 3096.900 \pm 0.006$ MeV. At this point, it is important to note that the Armenteros-Podolanski plots are 2D histograms which are not suitable for fitting. For this reason, the TProfile class of ROOT [21] is used as the profile histograms are characterized in many cases as an elegant replacement of two-dimensional histograms. Profile histograms are used to display the mean value of Y and its error for each bin in X. The displayed error is by default the standard error on the mean, i.e. the standard deviation divided by the $\sqrt{N}$. Using this method, the direct elimination of the third dimension is achieved, which presents the entries and enters of course in the profile histogram in a different way. What practically happens, using our 2D histogram as an example, a-pT, is that the resulting profile histogram retains the values of a on the x-axis, while the average values of the transverse momentum p_T of each bin are presented on the y-axis. Therefore, the information of the entries enters both in the calculation of the average value of p_T because $\overline{p_T} = \frac{\sum_{i=1}^{N} p_{T_i}}{N}$ as well as in the error of the average value, as we mentioned before, given by the equation $\sigma_{p_T} = \sqrt{\frac{\sum_{i=1}^{N}\left(p_{T_i} - \overline{p_T}\right)^2}{N}}$

All MC are used initially without any restriction on pseudorapidity η, resulting in:

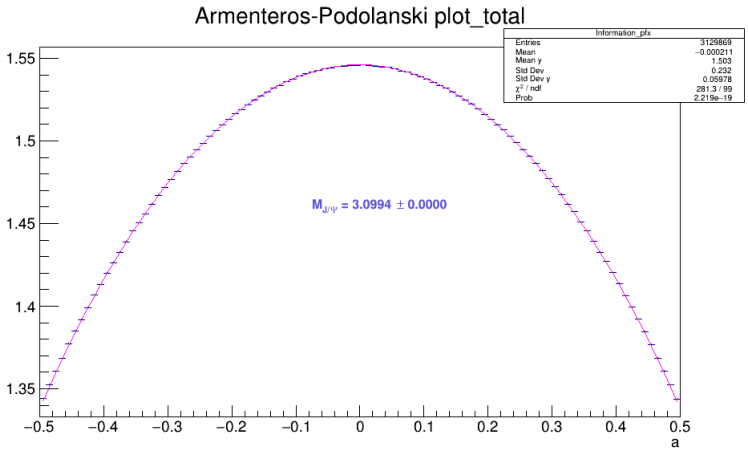

Figure 6.13: Profile of Armenteros-Podolanski plot without any η restriction

The mass parameter, which is returned by the ROOT, is not precise and neither the goodness-of-fit tests are successful. Knowing that the detector does not have the same resolution in all its parts, we create the following η regions from $[-1.1, 1.1]$ and separate our data according to the η region in which they are located:

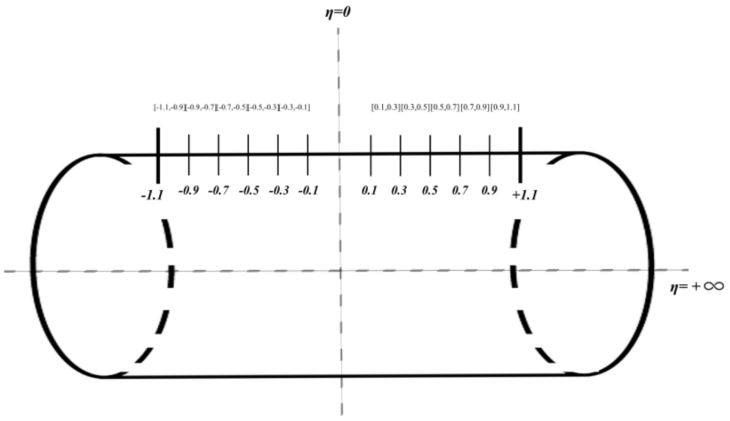

Figure 6.14: Separation of the detector into η-regions

Therefore, 11×11 plots are obtained. As an instance, one of the most successful fit is given:

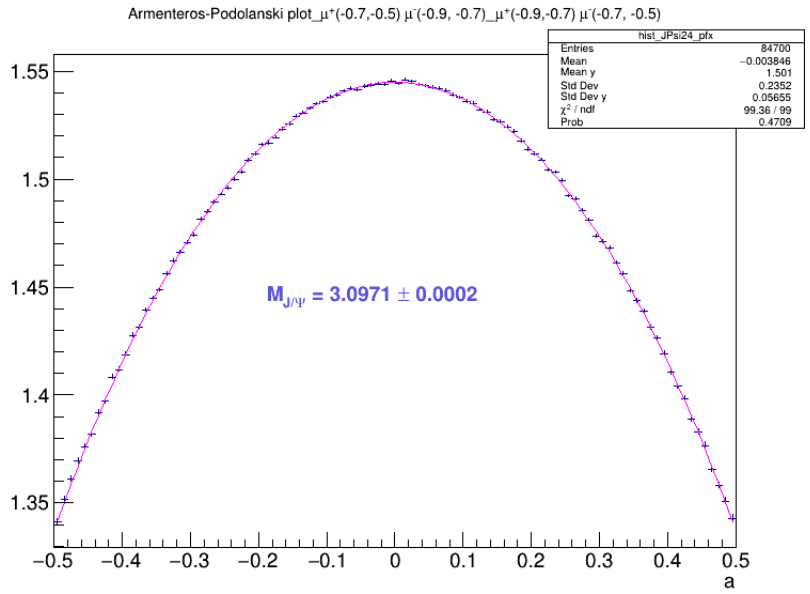

Figure 6.15: Profile of Armenteros-Podolanski plot for $\eta : (-0.7, -0.5)(-0.9, -0.7)$

With a general overview, it is observed that after the separation of the data into the η regions, the value of the J/ψ mass parameter, which is found from the fit, is more accurate than the total Armenteros-Podolanski plot, while in some regions it is almost exact. In addition, another result is that the muons from the J/ψ decay are produced close to each other, which is shown in the histogram below, Fig.6.16:

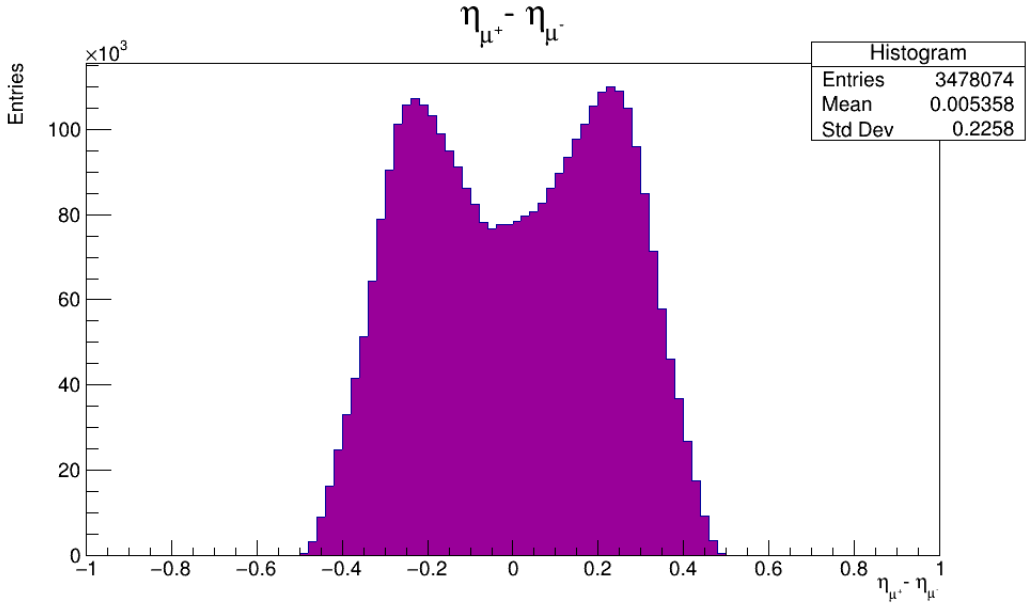

Figure 6.16: Difference between the pseudorapidity of the two muons: $\eta_{\mu+} - \eta_{\mu-}$

In order to comprehend these two observations, the inverse graphs are made. Initially, a graph is created to illustrate the number of muons produced per specific η-regions, which have been defined above.

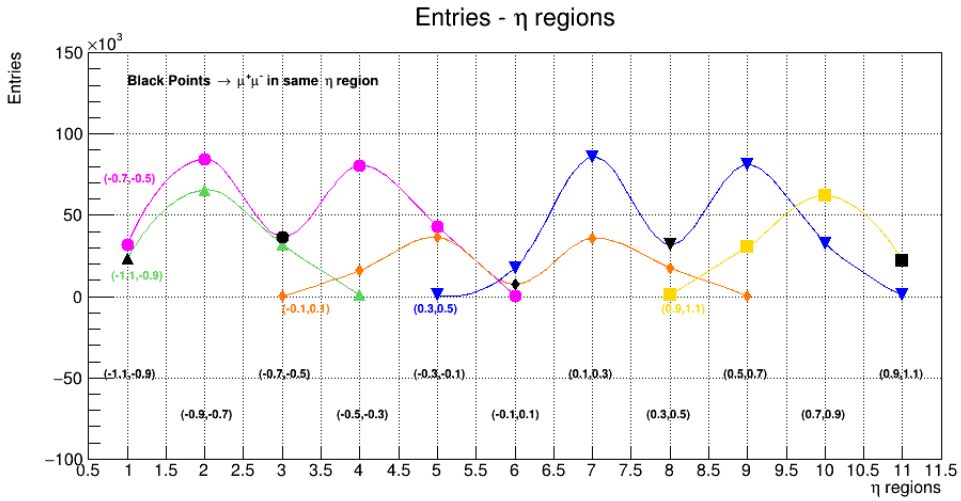

Figure 6.17: Entries per specific η regions of two muons from the J/ψ decay. Practically what we do is to select a reference η region each time and make all possible combinations with all the η regions. Indicatively, we draw some of these combinations so that the graph is distinct and can be analyzed. Each reference region is drawn in a different colour, while the η regions are marked in black

Observing the graph and studying each curve separately, we arrive at some common features. Firstly, the fewest entries, which can be used for statistical analysis, are observed when the two muons are produced in the same η region. For muons which are produced in the most distant η regions, the events are almost negligible, therefore they cannot be utilized in any statistical analysis. Moreover, from the graph it is obvious that most events occur when the muons are produced in adjacent regions, where we have the best statistics. Looking now at the graph as a whole, some curves are more elevated than others. For this reason, wanting to explore a little more the relevance of the entries to the η region, we create a histogram of muons' pseudorapidity η.

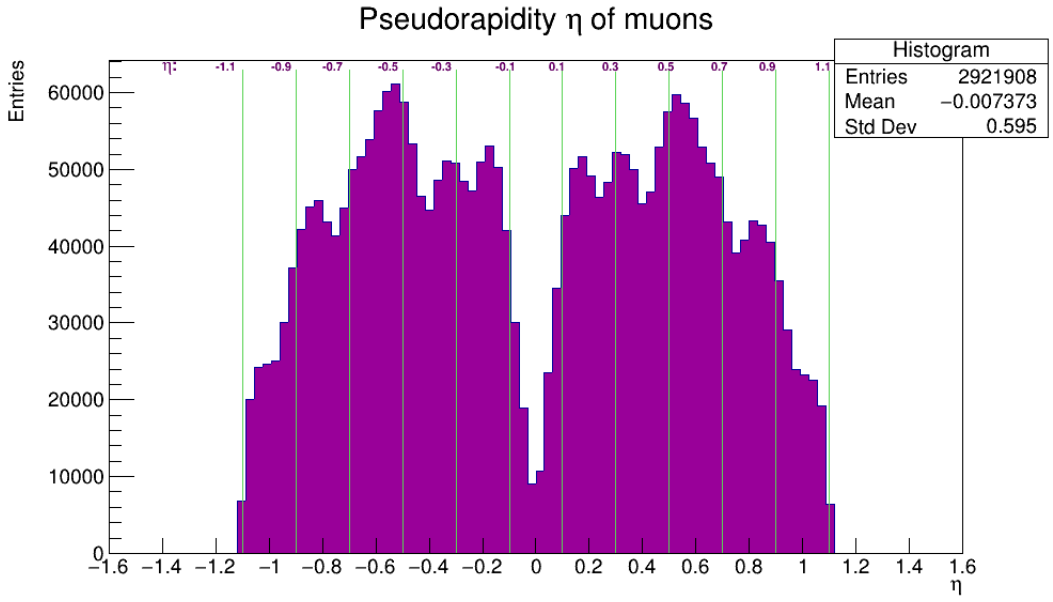

Figure 6.18: Histogram of muons' pseudorapidity η

The above histogram, Fig.(6.18), confirms what we already know, that our detector is not perfect. In some η regions it has better resolution while in others worse, which may be due to various reasons such as dead zones. Comparing the histograms Fig.(6.21) and Fig.(6.18), we observe that the curves which are more elevated, namely the blue and magenta ones, correspond to the regions with the most events, i.e., the regions (0.3,0.5) and (-0.7,-0.5) respectively. Furthermore, with a more general look at the histogram Fig.(6.18), we have a higher statistic in the central regions of the barrel compared to its outer regions.

Continuing with the other observation that was mentioned earlier regarding the fitted mass parameter, a graph with all the values of the fitted $M_{J/\psi}$ parameter is created. These values which are obtained from the various fits in the Armenteros-Podolanski plots for the different η regions. The same method of analysis is followed as in chapter 5, i.e. each time we assume that one of the two muons is found in a η region and the other one scans all η regions so that all possible combinations are made. The same procedure is repeated for all η regions. Schematically the methodology is:

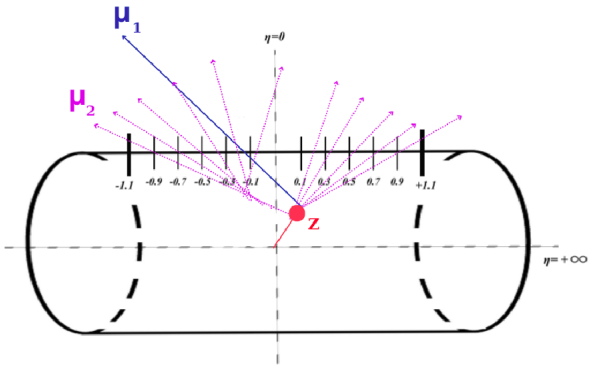

Figure 6.19: Schematically the followed methodology of analysis

It should be mentioned here that we do not use combinations that we have met before, as we are not interested in which of the two muons is detected in the η reference region, but only in the fact that one of the two muons is detected in it. Therefore, the combinations of η regions μ^+: (η_1, η_2) μ^-: (η_3, η_4) and μ^+: (η_3, η_4) μ^-: (η_1, η_2) are the same.

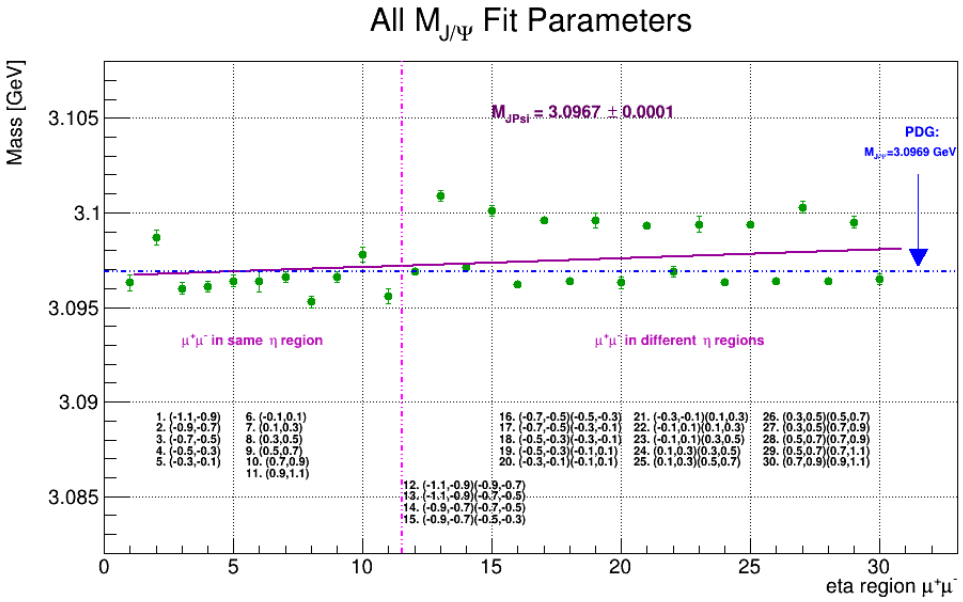

Figure 6.20: Fitted parameters of mass

At a first sight, a variation is observed in the mass values. In order to understand the reason for this variation we make two graphs with the number of events for each point in Fig.6.20.

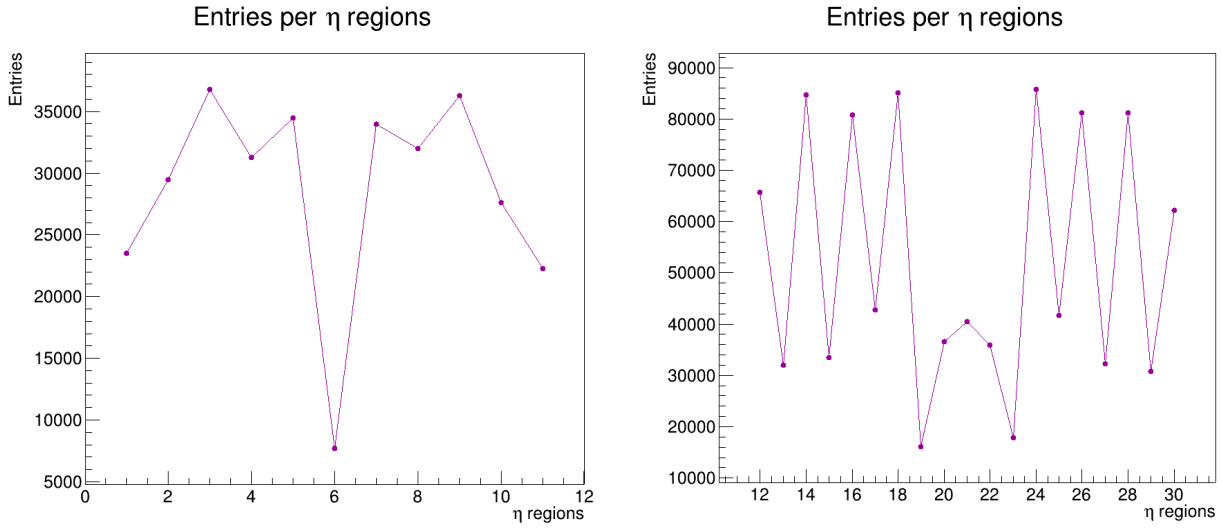

(a) Same η regions for $\mu^+\mu^-$

(b) Different η regions for $\mu^+\mu^-$

Figure 6.21: Entries per η regions

The left graph, Fig.6.21a, shows the number of events for the first 12 points of Fig.6.20 which refer to the case in which the two muons are in the same η region. This variation in the values of the mass parameter is due to a statistical error as variation in the number of events occurs, which is also revealed by Fig.6.18. Comparing now the two plots Fig.6.20 and Fig.6.21b with regard to the second part (points 12-30), i.e. for the case where the two muons are detected in different η regions, we observe a similar form, i.e. an up and down value shift. Therefore, this up and down of the mass values is justified by the fluctuation of the entries in Fig.6.21b. More events more accurate value, fewer events worse mass value. However this is not consistent with the histogram of pseudorapidity, Fig.6.18. For example, point 17 representing the η regions (-0.7,-0.5)(-0.3,-0.1) should be a point with good statistics which contradicts Fig.6.21b. The reason is that this variation in the mass values is not only due to statistical error but physics enters into it. Muons from J/ψ decay, as we have shown in Fig.6.16, are produced at short η distances. Moreover, from Fig.6.21 we had shown that higher statistics are observed when the two muons are produced in adjacent regions. This fact is the cause of the variation; for example, point 16, representing η regions (-0.7,-0.5)(-0.5,-0.3), has higher statistics as they are adjacent regions, while point 17, representing η regions (-0.7,-0.5)(-0.3,-0.1), which are close η regions but not adjacent, has lower statistics. Finally, by fitting the data with a first degree polynomial, where the constant term indicates the mass of J/Ψ, the mass parameter is found to be $M_{J/\Psi} = 3.0967 \pm 0.0001$, which is an accurate measurement.

6.5 Calibration Test

6.5.1 Methodology

The muon momentum scale and resolution obtained from the reconstruction of MC simulated events need to be corrected to reproduce with precision the characteristics of the muon momentum reconstructed in real data. The mass of a reconstructed $X \to ll$ (X being Z or J/ψ for example) is computed as:

$$m_{ll} = \sqrt{2E_1E_2\,(1 - cos(\theta_{12}))} \tag{6.22}$$

where E_1 and E_2 are the energies of the two leptons measured by the detector and θ_{12} is the opening angle between two leptons. Due to imperfect detector modeling is parametrised in the following way for a given region:

$$p_T^{meas} = p_T^{reco}\,(1 + a_i) \tag{6.23}$$

where p_T^{meas} is the measured lepton transverse momentum, p_T^{reco} is the reconstructed transverse momentum of the perfectly calibrated muons, and α_i represents the "departure" from a perfect calibration, in a given phase space region, for example pseudorapidity range, labelled i. Based on these relationships, the fisrt step is to perform different bins in η for both muons μ^+ and μ^-. Residual mis-calibration, due to imperfect detector modeling is parametrised in the following way for a given region:

$$E_i^{true} = E_i^{MC}\,(1 + a_i) \tag{6.24}$$

where the a_i is the calibration constant in the bin i. Therefore, the invariant mass of the muons for a category (i,j) is given by:

$$m_{ij}^{true} = \sqrt{2E_i^{true}E_j^{true}\,(1 - cos(\theta_{ij}))} \tag{6.25}$$

Neglecting second-order terms and assuming that the opening angle between the two leptons is perfectly measured, the effect on the di-lepton invariant mass is:

$$m_{ij}^{true} \approx m_{ij}^{reco}\left(1 + \frac{\alpha_i + \alpha_j}{2}\right) \tag{6.26}$$

Thus, we have:

$$m_{ij}^{true} = m_{ij}^{reco}\left(1 + \frac{\beta_{ij}}{2}\right)$$

with $\beta ij = \alpha_i + \alpha_j$.

Therefore, we will use this methodology to test whether the Armenteros-Podolanski plot is an effective calibration method. Practically, MC data are used and we modify them by a factor $1 + \alpha_i$ according to the η_i region where they are detected, as follows:

$$p_T^{meas} = p_T^{reco}\,(1 + a_i) \rightarrow p_T^{altered} = p_T^{original}\,(1 + a_i) \tag{6.27}$$

Then, by fitting the Armenteros-Podolanski plots of both original and altered MC data, the ratio $\frac{M^{alt.}}{M^{orig.}}$ is calculated and thus, according to the relation (6.26), it can be examined whether the experimental and theoretical values of $1 + \frac{\alpha_i + \alpha_j}{2}$ are consistent.

6.5.2 Same calibration constant α_i for the whole detector

The first identifying and simplest test for this methodology is to consider that the detector detects with the same ability in all its parts.

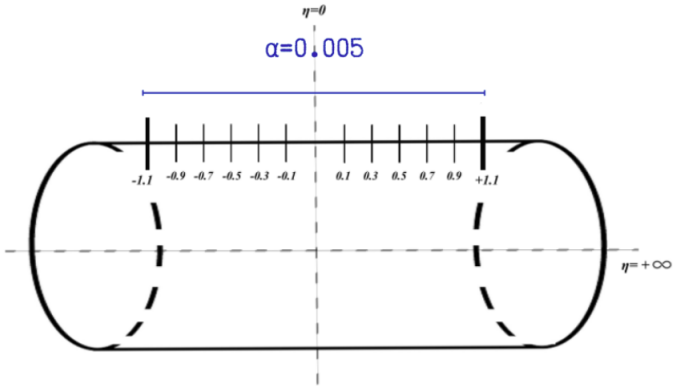

Figure 6.22: First calibration test, i.e. same calibration constant α_i for the whole detector

Thus, we generate pseudodata by changing the transverse momentum of the MC data by a factor of $1 + 0.005$, i.e.

$$p_T^{alt.} = p_T^{orig.}\,(1 + 0.005) \tag{6.28}$$

What we ideally expect, after finding the J/Ψ mass parameter from the fit to the Armenteros-Podolanski plots of both the original MC data and the pseudodata (altered MC), using the

relation (6.26), is:

$$M_{ij}^{alt.} = M_{ij}^{orig.}\left(1+\frac{\alpha_i+\alpha_j}{2}\right) \xLeftrightarrow{\alpha_i=\alpha_j=\alpha} \frac{M_{ij}^{alt.}}{M_{ij}^{orig.}} = 1+\frac{2\alpha}{2} \Leftrightarrow \frac{M^{alt.}}{M^{orig.}} = 1+\alpha = 1+0.005 \tag{6.29}$$

Observing all the graphs, the results are very satisfactory. Indicatively, the following is provided:

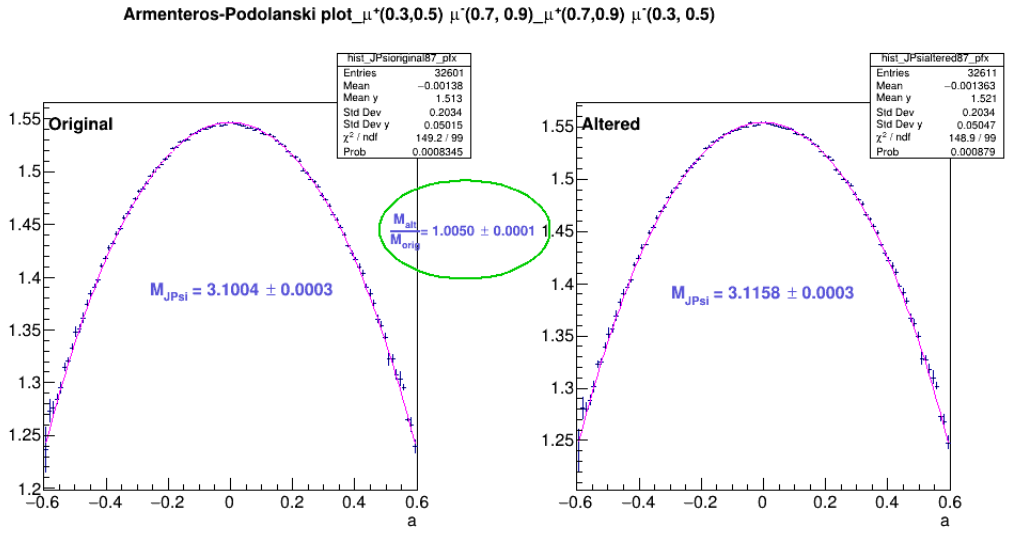

Figure 6.23: Armenteros-Podolanski plot of the original and altered MC data in η regions (0.3,0.5)(0.7,0.9)

To obtain an overall picture we create a graph with all the results and so:

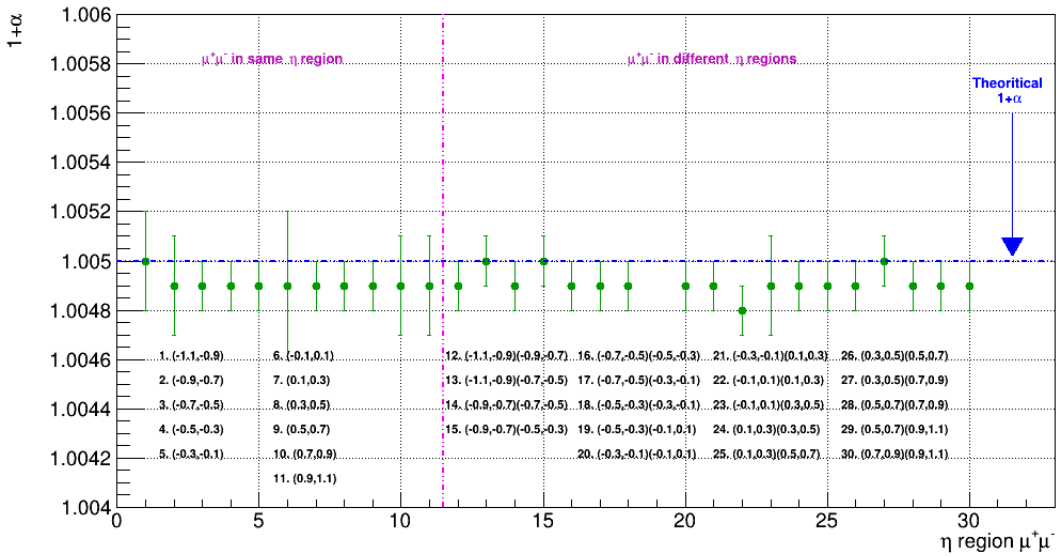

Figure 6.24: The factor $1 + \alpha$ from all η regions

However, we cannot overlook the fact that essentially the same events are used in both Armenteros-Podolanski plots as the altered MC data (pseudodata) have been generated by a change in the transverse momentum of the original MC data by a factor of $1 + 0.005$.

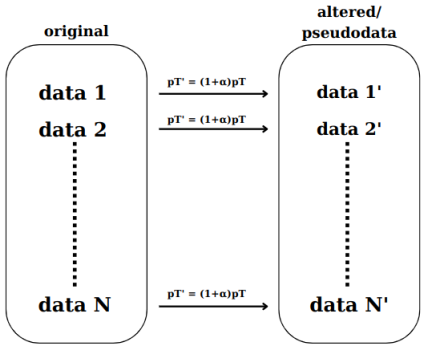

Figure 6.25: The method of generating pseudodata

Therefore, wanting to obtain the randomness of the events we split the events in both cases in half and use the different halves of the MC data to create the corresponding Armenteros-Podolanski plots, as shown in the figure below (fig.6.26):

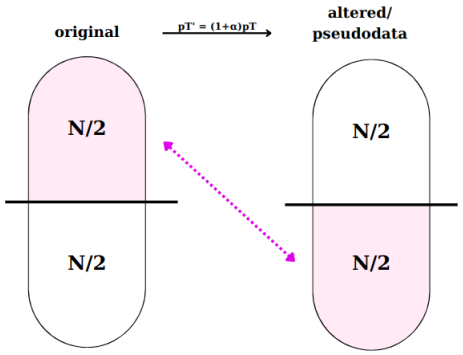

Figure 6.26: The method of generating pseudodata and the selection made to increase the randomness

and following the same procedure we get the results below:

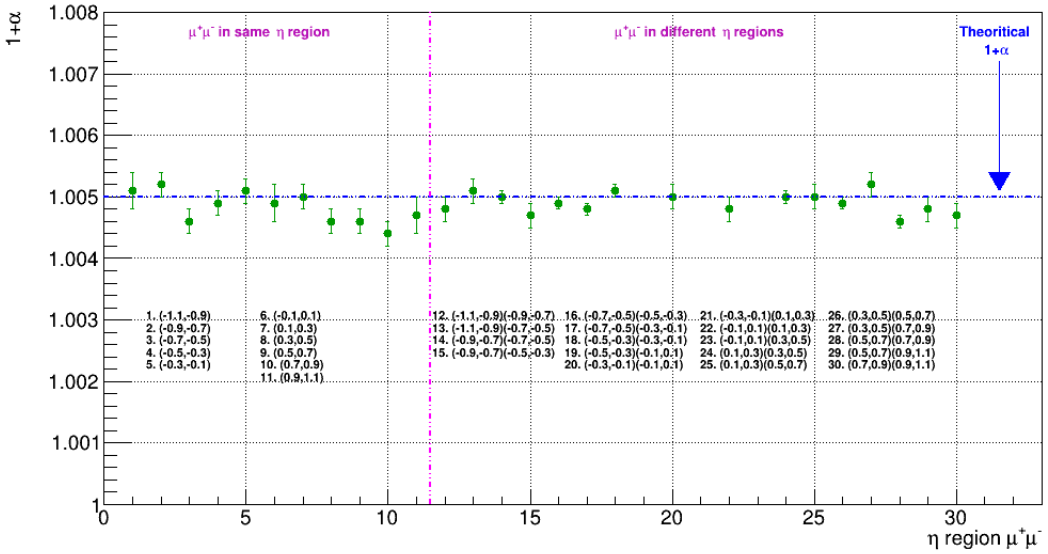

Figure 6.27: The factor $1+\alpha$ from all η regions, using half entries

In this case too, it is observed that the results are consistent with the theoretical value $1+\alpha = 1+0.005$.

6.5.3 Different calibration constant α_i in each η_i region

The previous test gave encouraging results but we should be aware that this test refers to an idealized and simplified scenario, as the detector does not detect with the same efficiency in all its parts. Therefore, the next step is to take into account the real conditions, i.e. each

η_i region is characterized by a different calibration constant, α_i. Thus, we define arbitrary calibration constants, α_i for each region, which are shown in the figure below:

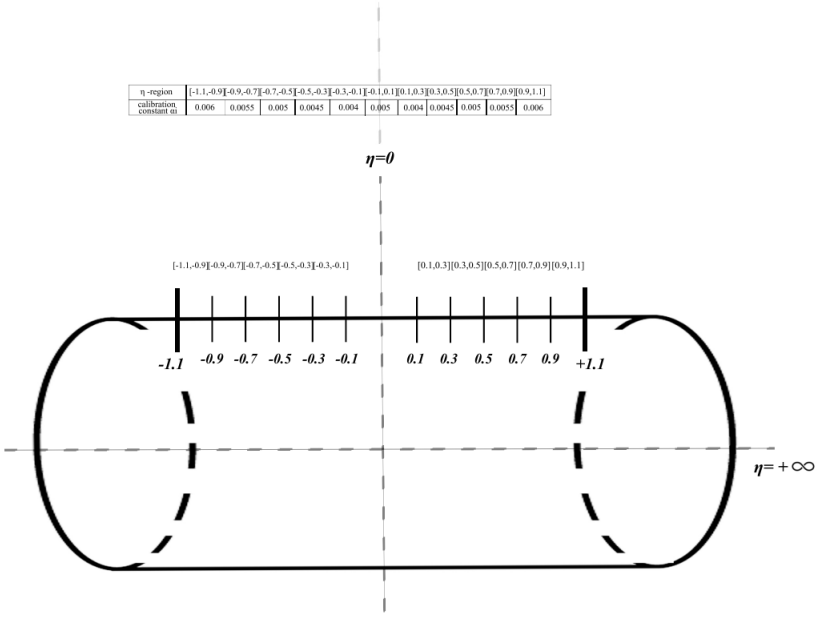

Figure 6.28: The calibration constants α_i for each η_i region

Having defined the calibration constants, the pseudodata are produced by changing their transverse momentum as previously:

$$p_T^{alt.} = p_T^{orig.}\,(1 + \alpha_i)$$

where α_i is the calibration constant characterizing the η_i region in which each muon is detected.

To obtain an overall view of the results, we create a graph of the difference between the value that is found and the corresponding theoretical value of the quantity $1+\frac{\beta_{ij}}{2} = 1+\frac{\alpha_i+\alpha_j}{2}$ as a function of the η region and so we have:

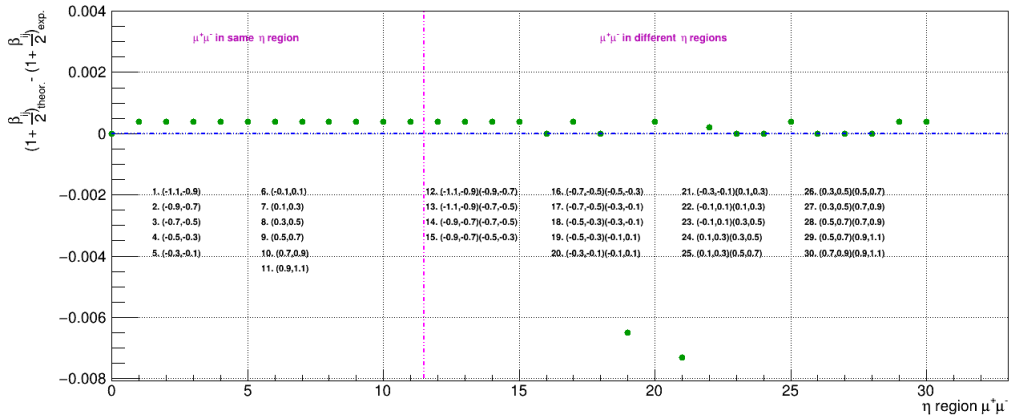

Figure 6.29: The factor $1+\alpha$ from all η regions

It is obvious from the graph that the difference is very small. Moreover, for some specific values the difference is zero, as for example in point 16 where it refers to the ranges (0.7,-0.5)(-0.5,-0.3). Continuing with exactly the same procedure which is followed in the previous test, to increase randomness we split the data in half and use half of them as the original events and the other half to create the pseudodata (Fig.6.26). Thus:

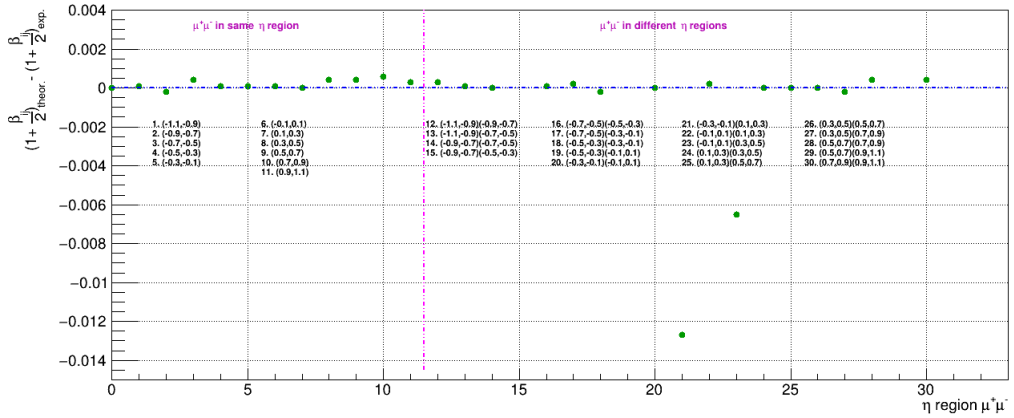

Figure 6.30: The factor $1+\alpha$ from all η regions, using half entries

The results in this case are also very encouraging because through the Armenteros-Podolanski plot the experimental value of the quantity $1+\frac{\alpha_i+\alpha_j}{2}$ is calculated quite close to its theoretical value and for this reason their difference is close to zero for almost all η regions, as shown in Fig. (6.30).

Chapter 7

Conclusions

The thesis focused on the study of the mass of the boson Z and the meson J/ψ. The first part of the analysis, which was elaborated in chapter 5, aimed at examining the mass distribution of Z in order to find the functions that describe it. Initially, Monte Carlo (MC) data was used to create the mass histogram and after several attempts and combinations of functions it was found that a Crystal Ball and a Gaussian function satisfactorily described the signal while a second degree Chebyshev polynomial was used for the background. Although the fit was visually compatible with the mass distribution, the goodness-of-fit tests revealed the opposite, i.e. a bad fit. Therefore, the fit procedure needed improvement. So, the idea based on the fact that the detector does not have the same resolution in all its parts was applied, to use an additional criterion in our data, the criterion of the pseudorapidity (η). We therefore divide the detector into 11 η-regions between the limits [-1. 1,1.1] and because each of the two produced muons can be detected in one of these regions, 11×11 mass histograms were made satisfying all possible combinations of η-regions between the two muons. This idea was successful because by making this separation, the fit procedure was significantly improved in all histograms. Examining the results a little further, it was observed that this separation affects the statistics. In particular, it was found that the least data for analysis are recorded when both muons are produced in the same η region, while the most ones when they are detected in adjacent η regions. As the two muons become more distant from each other, i.e., as the angle between them increases, there is a gradual small decrease in the number of events. Moreover, studying the values of the fitted parameters, mass and σ, it is observed that there is a variation with a more intense one in the parameter σ. Analyzing the fitted mass parameters further, we conclude that this variation reveals a systematic error. In particular, more accurate mass values were found in the central regions of the detector compared to the more outer regions of the barrel, which is probably due to a

bad reconstruction when muons are produced in the edges of the barrel, i.e. when they are produced at bigger angles. After having completed the analysis on the MC, is applied the same model and the same methodology to the data in order to compare the results between them. We therefore conclude first that the same significant improvement in the fit procedure occurs when the data are divided into the same η regions, and second that this separation has the same effect on the statistics. However, when we proceed to analyse the impact of the separation of the η regions on the fitted parameters, although there is again an intense variation in the fitted parameter σ, the image for the mass parameter does not reveal similar behaviour. In particular, the graph with all the fitted mass values using the data is different from that of MC because the variation in this case is unobservable. Therefore, there is no systematic error indicated in the data. This difference in the results of the mass parameter indicates that the MC probably need some corrections. Finally, a general impression on the programming part is that the fit procedure is a complex process as mentioned in chapter 5 because the fit is done by minimizing the least-square or likelihood function, which creates many difficulties. Therefore, in order to succeed the fit procedure on many histograms, such as in our case where 11×11 mass histograms were created on both data and MC, it is necessary to initialize the fitted parameters appropriately and at the same time to set suitable limits on them.

In the second part of the analysis a new calibration method is proposed based on the Armenteros-Podolanski plots. The motivation for this study comes from the attempt to precisely measure the mass of the Z boson. The pursuit of an accurate measurement has led the studies to focus on improving the calibration of muon momentum. Due to the fact that our object of study is the Z boson, the calibration will be performed on J/ψ. The Armenteros-Podolanski plot, as it was mentioned previously, is a representation of the transverse momentum of a two-body decay versus the asymmetry of the longitudinal momentum of the decay products. In this space two-body decays appear as semi-ellipses, whose parameters provide information on the masses of the parent and the child particles. In order to examine whether the Armenteros-Podolanski plots can be used to calibrate the detector, we applied to them three tests from which we had very satisfactory and encouraging results for further study of this methodology as a new way of calibration. These tests are based on the fit procedure to the ellipses observed in the J/ψ data as in this way the masses of the muons and J/ψ can be retrieved. The first test is simply the fit procedure to the Armenteros-Podolanski plots using the MC data of J/ψ. However, using all the data both the fitted parameter of mass and the goodness-of-fit tests are not satisfactory. For this reason, proceeding with the similar idea that regulates the whole previous analysis, the data are divided according

to their pseudorapidity η. By dividing the detector into 11 regions between the η limits [-1.1,1.1], 11×11 Armenteros-Podolanski plots and their corresponding fits are generated. The fit procedure had significant improvement for all plots. Some remarkable results came out of this process. First, the muons from the decay of J/ψ are produced close to each other, i.e. with a small angle between them. In particular, when the two muons are produced in the same region we have the least number of events for analysis, while the highest statistics is obtained when the two muons are located in adjacent regions. For larger distances between the muons the events are almost zero. This separation also revealed a statistical error as it is already known that the detector is not perfect and therefore it does not detect with the same resolution in all parts. Thus, in some η regions the statistics is higher. For this reason, the fitted parameters of mass obtained from the fit procedure when the muons are detected in the same η region are quite accurate for the η regions with high statistics. Next, examining all the fitted parameters of the mass for muons that are not produced in the same η regions, there is an up and down shift of values that reveals a statistical error. The causes of the error are physics itself. When the muons are produced in adjacent η regions, most events are observed and therefore the measurements are quite good, while if the η distance is increased a little more, the events decrease significantly and the measurements are moved away from the reference value of PDG. Finally, by fitting the data with a first degree polynomial, where the constant term indicates the mass of J/ψ, the mass fitted parameter is found to be $M_{J/\psi}$ $= 3.0967 \pm 0.0001$ GeV, which is an accurate measurement. The second and third tests, also known as the calibration tests, are based on the imperfect detector modelling. Using this model, we generate from the MC original data the pseudodata as follows:

$$p_T^{altered} = p_T^{original}\,(1 + a_i) \tag{7.1}$$

where α_i is the calibration constant.
Then, by fitting the Armenteros-Podolanski plots of both original and altered (pseudodata) MC data, the ratio $\frac{M^{alt.}}{M^{orig.}}$, which equals to the quantity $1 + \frac{\alpha_i+\alpha_j}{2}$, is calculated and thus it can be examined whether the experimental and theoretical values of $1+\frac{\alpha_i+\alpha_j}{2}$ are consistent. Specifically, the second test, which is the most simplified because it assumes that the detector has the same resolution in all its parts, i.e. $\alpha_i = \alpha_j = \alpha$, was an identification test. After we have obtained satisfactory results, we proceeded to the 3rd test, which describes the real condition, i.e. that the detector does not detect with the same ability in all its parts. So the same procedure was repeated but this time with different calibration constants for each η region. The results in this case are also very satisfactory. Therefore, through this analysis we have encouraging indications for further research and this allows us to believe that it can be used as a new calibration method. A general impression regarding the programming of

the fit procedure for the Armenteros-Podolanski plots is that it was a much more simplified procedure than the classical process of fitting to the mass distribution of every single particle - in our case the boson Z - as it did not require much effort in initializing the parameters nor a complex code to achieve the fit to 11×11 histograms.

List of Figures

References

[1] Mark Thomson. *Modern particle physics*. Cambridge University Press, 2013.

[2] David Griffiths. *Introduction to elementary particles*. John Wiley & Sons, 2020.

[3] Francis Halzen and Alan D Martin. *Quark & Leptons: An introductory course in modern particle physics*. John Wiley & Sons, 2008.

[4] https://www.home.cern/.

[5] https://home.cern/science/experiments.

[6] The ATLAS Collaboration. The atlas experiment at the cern large hadron collider. *Jinst*, 3:S08003, 2008.

[7] The ATLAS Collaboration. *ATLAS detector and physics performance: Technical Design Report, 1*. Number CERN-LHCC-99-014. ATLAS-TDR-014, 1999.

[8] ATLAS. *Magnet system: Technical Design Report, 1*. CERN, Geneva, 1997.

[9] Joshua R Klein and Aaron Roodman. Blind analysis in nuclear and particle physics. *Annu. Rev. Nucl. Part. Sci.*, 55:141–163, 2005.

[10] Ιωάννης Δ. Βέργαδος, Σμαράγδα Δ. Λώλα, Ηλίας Σ. Τριανταφυλλόπουλος. *Εισαγωγή στα στοιχειώδη σωμάτια - Κοσμολογία*. Συμμετρία, 2015.

[11] Fred James. Function minimization. 1972.

[12] https://indico.desy.de/event/13610/contributions/13668/attachments/9228/10835/RooFit_Tutorial_Desy2016.pdf.

[13] Glen Cowan. *Statistical data analysis*. Oxford university press, 1998.

[14] Frederick James. *Statistical methods in experimental physics*. World Scientific Publishing Company, 2006.

[15] Bevington PR and DK Robinson. Data reduction and error analysis for the physical sciences. *MeGraw-I-Iill, New York*, 1969.

[16] Atlas Collaboration et al. Measurements of W and Z boson production in *pp* collisions at $\sqrt{s} = 5.02$ TeV with the ATLAS detector. *arXiv: 1810.08424*, 2018.

[17] CDF Collaboration†‡, et al. High-precision measurement of the W boson mass with the CDF II detector. *Science*, 376(6589):170–176, 2022.

[18] P Baladrón Rodríguez, Veronika Chobanova, X Cid Vidal, Vladimir Gligorov, M Lucio Martínez, Jovan Markov, D Martínez Santos, and M Pló Casasús. Calibration of the momentum scale of a particle physics detector using the Armenteros-Podolanski plot. *Journal of Instrumentation*, 16(06):P06036, 2021.

[19] J Podolanski and R Armenteros. III. Analysis of V-events. *The London, Edinburgh, and Dublin Philosophical Magazine and Journal of Science*, 45(360):13–30, 1954.

[20] Θεόδωρος Αλεξόπουλος, Γεώργιος Τσιπολίτης. *Προβλήματα Φυσικής - Μηχανική*. ΕΜΠ, 2004.

[21] https://root.cern.ch/doc/master/classTProfile.html.